The dynamical control of subduction parameters on surface topography

F. Crameri[1,2] iD, **C.R. Lithgow-Bertelloni[2]** iD, **and P.J. Tackley[3]** iD

[1]Centre for Earth Evolution and Dynamics (CEED), University of Oslo, Oslo, Norway, [2]Department of Earth Sciences, University College London, London, UK, [3]Department of Earth Sciences, ETH Zurich, Zurich, Switzerland

Abstract The long-wavelength surface deflection of Earth's outermost rocky shell is mainly controlled by large-scale dynamic processes like isostasy or mantle flow. The largest topographic amplitudes are therefore observed at plate boundaries due to the presence of large thermal heterogeneities and strong tectonic forces. Distinct vertical surface deflections are particularly apparent at convergent plate boundaries mostly due to the convergence and asymmetric sinking of the plates. Having a mantle convection model with a free surface that is able to reproduce both realistic single-sided subduction and long-wavelength surface topography self-consistently, we are now able to better investigate this interaction. We separate the topographic signal into distinct features and quantify the individual topographic contribution of several controlling subduction parameters. Results are diagnosed by splitting the topographic signal into isostatic and residual components, and by considering various physical aspects like viscous dissipation during plate bending. Performing several systematic suites of experiments, we are then able to quantify the topographic impact of the buoyancy, rheology, and geometry of the subduction-zone system to each and every topographic feature at a subduction zone and to provide corresponding scaling laws. We identify slab dip and, slightly less importantly, slab buoyancy as the major agents controlling surface topography at subduction zones on Earth. Only the island-arc high and the back-arc depression extent are mainly controlled by plate strength. Overall, his modeling study sets the basis to better constrain deep-seated mantle structures and their physical properties via the observed surface topography on present-day Earth and back through time.

Plain Language Summary Earth's partially molten mantle flows over millions of years due to the high temperatures, the enormous pressures and the tiny defects in crystals that occur in the Earth's rocky interior. This global flow of mantle material, in particular in regions where cold, heavy plates sink back into the mantle (i.e., subduction), causes visible variations of surface elevation. These topographic variations potentially allow us to better understand the hidden structures and dynamics in Earth's interior. We have developed an efficient model of Earth's interior and can therefore run numerical experiments to better understand this interaction of mantle flow and surface topography. We test the numerous, to some extend still unknown, dynamic, rheologic and geometric properties of subduction zones and quantify their potential to deflect the plate at the surface. We find that the angle of the sinking plates and their relative weight compared to their surrounding have a major control on lifting and depressing the plate surface. Our results will finally allow us to better understand the interior of a planet on present day, but also back through time by simply looking at either the present surface topography or at the available data back through geologic time.

1. Introduction

Sinking slabs are the largest lateral mass anomalies in the Earth. These veteran portions of surface plates are cold and heavy and, consequently, the most important drivers of both mobile-lid plate tectonics [*Forsyth and Uyeda*, 1975; *Conrad and Lithgow-Bertelloni*, 2002] and flow in the surrounding mantle [e.g., *Funiciello et al.*, 2003; *Crameri and Tackley*, 2014]. Therefore not surprisingly, their excess weight also causes the Earth's surface to deflect [e.g., *Davies*, 1981]. Earth's topography, which is easily measurable by human beings, is therefore a crucial and, in fact, the most direct observable we have on the internal dynamics of the planet.

The dynamic link between a deep slab and the plate surface is twofold: first, stresses are transmitted along the high-viscosity slab [*Elsasser*, 1971]; second, stresses are transmitted through the low-viscosity mantle

wedge [e.g., *Mitrovica et al.*, 1989]. The primary fraction of surface topography originates, however, from forcing produced within the lithosphere: horizontal lithospheric compression or extension and the isostatic compensation of lateral differences in lithospheric density and thickness cause a well-understood surface deflection with amplitudes of the order of around ±6 km. Yet, there is still a considerable discussion about the actual elevation contrasts arising due to deep-seated sources like slabs. Indication for such a deeply sourced surface-deflection component comes from residual seafloor topography [*Cazenave et al.*, 1989; *Davies and Pribac*, 1993], anomalously depressed continental hypsometry [*Gurnis*, 1993; *Dávila et al.*, 2010], and from geoid measurements and mantle tomography [*Hager et al.*, 1985]. The proposed amplitude of such a long-wavelength "dynamic" component of topography varies between a few hundreds of meters [e.g., *Ribe and Christensen*, 1994; *Le Stunff and Ricard*, 1995; *Ribe and Christensen*, 1999; *Wheeler and White*, 2002; *Kaban et al.*, 2004; *Braun*, 2010; *Orth and Solomatov*, 2012; *François et al.*, 2014; *Hoggard et al.*, 2016] and up to >1 km [e.g., *Forte et al.*, 1993; *Lithgow-Bertelloni and Silver*, 1998; *Moucha et al.*, 2009; *Boschi et al.*, 2010; *Forte et al.*, 2010; *Liu and Gurnis*, 2010; *Moucha and Forte*, 2011; *Flament et al.*, 2013; *Gurnis*, 1993; *Flament*, 2014; *Husson et al.*, 2014].

The observed topography at a destructive ocean-ocean convergence zone can generally be characterized by four prominent, regional (i.e., 50−1000 km wide) features [see e.g., *Zhong and Gurnis*, 1994]: From the subducting plate to the overriding plate these features are (i) outer rise (or viscous fore-bulge), (ii) subduction trench, (iii) island-arc (or volcanic arc), and (iv) back-arc depression (or basin). Each of these accurately observable topographic characteristics possibly constrain in its own way parts of the deep-seated subduction dynamics as they appear to be mainly controlled by a suite of subduction parameters.

Such previously identified subduction parameters with a strong confirmed correlation to surface topographic features are, for example, shallow-depth slab dip, slab age, and slab-pull force. These and other subduction parameters influencing surface topography can be merged to three key physical aspects: (i) Buoyancy, or the driving forces of subduction, (ii) rheology, or the resisting forces of subduction, and (iii) geometry, or the location and hence direction of the forcing.

First, there are several important parameters controlling the *buoyancy* within the subduction system and its impact on surface topography. The slab's buoyancy is mainly controlled by its composition and temperature. The slab's temperature is, in turn, mainly controlled by the age of the plate during subduction [see e.g., *Vlaar and Wortel*, 1976; *Jarrard*, 1986], which has been found to correlate with the depth of the subduction trench [*Hilde and Uyeda*, 1983; *Jarrard*, 1986; *Zhong and Gurnis*, 1992; *Gurnis et al.*, 1996] and upper plate strain [*Jarrard*, 1986; *Lallemand et al.*, 2005].

Second, there are several important *rheological* complexities of the subduction system that ultimately impact surface topography. The viscous dissipation inside the lithosphere during bending at the trench or the friction at the plate interface along the subduction fault and in the subduction channel produce forcing that opposes subduction [*Conrad and Hager*, 1999] and hence might reduce topographic amplitudes. Moreover, the transmission of deep, slab-induced forcing to the surface is strongly controlled by the slab's surrounding medium. Therefore, mantle viscosity is likely another crucial rheological parameter controlling surface deflection. A low-viscosity mantle wedge has indeed been shown to reduce the depression in the back-arc [*Billen and Gurnis*, 2001; *Billen et al.*, 2003]. Additionally, *Zhong and Gurnis* [1992] showed that a sufficiently high slab-mantle viscosity contrast is needed to produce a narrow and deep trench.

Third, there are several important *geometrical* complexities of a subduction system impacting surface topography. One crucial geometric aspect that could be constrained by surface topography is the dip angle of shallow slabs: The shallow-depth dip angle of subduction zones (i.e., the angle between the shallow, subducting slab and the Earth's surface) varies significantly between separate subduction zones, and even along the same subduction zone [*Isacks and Barazangi*, 1977; *Jarrard*, 1986; *Cruciani et al.*, 2005; *Lallemand et al.*, 2005]. Flat subduction is for example observed in central Chile [*Stauder*, 1973; *Barazangi and Isacks*, 1976] and Central Mexico [e.g., *Suarez et al.*, 1990; *Pérez-Campos et al.*, 2008]. There, the shallow flat slab segments are connected to steeper-dipping portions further down the subduction zone and also to their side, and might explain the anomalously large and deep sedimentary basins in the Argentine Pampas [*Dávila et al.*, 2010]. The negative buoyancy of shallow-lying slabs has been shown to be transmitted rather through the mantle wedge than along the slab [*Elsasser*, 1971], which, in fact, causes a deeper topographic depression in the back-arc [*Gurnis et al.*, 1996]. Additionally, upper plate strain is found to correlate with the

shallow-depth slab dip angle [*Jarrard*, 1986; *Lallemand et al.*, 2005]. Shallow-dipping slabs have further been shown to correlate with shallow trenches [*Hilde and Uyeda*, 1983; *Jarrard*, 1986].

Such time and space-dependent changes in buoyancy, rheology, and geometry of a subduction system crucially deflect the plate surface. These surface deflections then can cause dramatic time-dependent inundation [*Gurnis*, 1993; *Russell and Gurnis*, 1994; *Liu et al.*, 2008; *Dávila et al.*, 2010; *Jones et al.*, 2011] and even whole river-system reorganizations [*Eakin et al.*, 2014] on the continental scale. Such widespread, important topographic consequences motivated many modeling studies focussing on variable subduction dynamics, like for example flat slabs [*Mitrovica et al.*, 1989; *Zhong and Gurnis*, 1992, 1994; *van Hunen et al.*, 2004; *Manea et al.*, 2012; *Rodríguez-González et al.*, 2012; *Arrial and Billen*, 2013; *Jadamec et al.*, 2013; *Dávila and Lithgow-Bertelloni*, 2015; *Gérault et al.*, 2015; *Taramón et al.*, 2015; *Hu et al.*, 2016; *Hu and Liu*, 2016]. Moreover, the surface-topography variation induced by variable subduction dynamics represents a rare opportunity to systematically explore subduction systems of the past. Yet, there is no comprehensive, systematic study on the relative importance of all the different key aspects of a subduction system (i.e., buoyancy, rheology, and geometry) to deflect the plate surface, while considering the individual regional topography features.

This study, focussing on the dynamic link between slab forcing and rock-air interface deflection, aims therefore at considering all three key aspects of the subduction system and their individual impact on each and every topography feature, while using an appropriately simplified geodynamic model: Recent numerical advances allow us to model global, mobile-lid mantle convection in combination with a free top surface [*Crameri et al.*, 2012a] and to reproduce dynamically fully self-consistent, realistic, single-sided subduction [*Crameri et al.*, 2012b]. It is difficult to fully control the state of a subduction zone in a model that is dynamical self-consistent. Here, this model is therefore run for only 2 Ma, which removes some of the self-consistency and gives us sufficient control over the subduction zone's physical state via the artificial initial condition. In the remainder of this paper, we are therefore able to unravel the individual impact of various physical complexities that control a subduction system's buoyancy, rheology, and/or geometry and that are involved in producing, transmitting, and filtering the *dynamic*, topographic signal of subduction.

2. Methods

We use here a simple, viscoplastic numerical model of global mantle convection that can reproduce dynamically self-consistent single-sided subduction [*Crameri and Tackley*, 2015] and that is run for a short time period of 2 Ma and controlled by the initial condition. For this study, the model has been developed further to produce reliable topography signals with a resolution down to only a few tens of meters. The detailed physical and numerical aspects of the model as well as the fully automated diagnostics of the postprocessing and additional methodology are described below. To prevent the most-common scientific visualization pitfall, we do *not* use the rainbow colormap [see e.g., *Borland and Ii*, 2007].

2.1. Physical Model

We here model an incompressible mantle under the Boussinesq approximation, for which the relevant non-dimensional equations for conservation of mass, momentum, and energy are:

$$\vec{\nabla} \cdot \vec{v} = 0 \tag{1}$$

$$\vec{\nabla} \cdot \sigma_{ij} - \vec{\nabla} p = RaT\hat{e}_z \tag{2}$$

$$\frac{\partial T}{\partial t} = \nabla^2 T - \vec{v} \cdot \vec{\nabla} T + H \tag{3}$$

where v is the velocity, σ_{ij} is the deviatoric stress tensor, p the pressure, T the temperature, $\hat{e}_z$ the vertical unit vector, t the time, and H the nondimensional internal heating rate. The temperature-based Rayleigh number (Ra) can be expressed in terms of density (ρ), gravitational acceleration (g), temperature scale (ΔT), mantle depth (D), thermal diffusivity (κ), and reference viscosity (η_0) as

$$Ra = \frac{\rho g \alpha \Delta T D^3}{\eta_0 \kappa} \tag{4}$$

The applied temperature-based Rayleigh number is 10^6 and the nondimensional internal heating rate is 20.0, which gives an internal heating-based Rayleigh number of 2.0×10^7. This value is at the lower end of

what is expected to be the case for Earth's mantle. To account for that, we normalize our results to the characteristic plate thickness. The assumed rheology is strongly temperature and pressure-dependent:

$$\eta(T, p) = \eta_A \cdot \exp\left[\frac{E_{act} + pV_{act}}{RT}\right] \tag{5}$$

where η is the viscosity, p is the pressure, $R = 8.314$ Jmol^{-1} K^{-1} is the gas constant, T the temperature, $E_{act} = 240$ kJ/mol the activation energy, V_{act} the varied activation volume, and η_A is set such that η gives the reference viscosity (η_0) at $T = 1600$ K and $p = 0$ Pa. Additionally, plastic yielding is included by a yield stress limiter using a Drucker-Prager yield criterion with the pressure-dependent yield stress $\sigma_{y,brittle}$ based on Byerlee's law

$$\sigma_{y,brittle} = C + p\mu \tag{6}$$

with specified friction coefficient μ and cohesion C. We additionally apply a maximum, ductile yield stress given by

$$\sigma_{y,ductile} = \sigma_{y,const} + \Delta\sigma_y \cdot d \tag{7}$$

where $\sigma_{y,const}$ is the surface value of the ductile yield stress, $\Delta\sigma_y$ is the ductile yield stress gradient, which is here set to zero for simplicity, and d is the nondimensional depth ranging from 0 (top) to 1 (bottom). The effective yield stress is then given by

$$\sigma_y = \min\left[\sigma_{y,brittle}, \sigma_{y,ductile}\right] \tag{8}$$

with a crossover between brittle and ductile yielding occurring in the lower part of the lithosphere (i.e., here 72 km). To consistently represent results in this study, we further define a mean yield strength over a certain depth range, $z_1 - z_2$, with

$$\sigma_{y,mean} = \frac{1}{z_2 - z_1} \int_{z_1}^{z_2} \sigma_y(z)\, dz \tag{9}$$

If plastic yielding occurs, the effective viscosity on the corresponding grid points becomes $\eta_{eff} = \min[\eta(T, p), \eta_y]$ with $\eta_y = \sigma_y/(2\dot{\varepsilon})$, where $\dot{\varepsilon}$ is the strain rate. Finally, the viscosity variation is limited to nine orders of magnitude by applying an upper and lower cut-off of $\eta_{max} = 10^5\eta_0$ and $\eta_{min} = 10^{-4}\eta_0$.

A weak hydrated crustal layer is initially included on top of the subducting plate (for detailed tests see *Crameri and Tackley* [2015]). The weak crustal layer is initially $d_{crust} = 15$ km thick and differs from mantle material only in a lower yield strength with $\mu_{crust} = 0.001$. The control model in this study assumes an isoviscous mantle underneath a higher-viscosity plate. Given the fact that we only run models for 2 Ma with only a shallow slab, we consider this setup the optimal (and simplest) starting point for systematic parameter tests. However, previous studies showed that a higher-viscosity lower mantle is crucial to reproduce realistic slab deformation for on-going subduction [e.g., *Garel et al.*, 2014]. We therefore test the effects of variable radial mantle viscosity carefully with additional setups.

The model spanning the whole depth down to the core-mantle boundary is purely internally heated (using an internal heating rate of 5.44×10^{-12} W/kg). The top boundary (including the air layer, if applied) is set to a constant 300 K, while the bottom boundary is insulated by applying a zero heat-flux condition. All model-domain boundaries are free-slip (whereas the actual rocky surface can be allowed to be a free surface by adding an air layer on top as mentioned below). The side boundaries are vertical free-slip walls, which do not significantly interfere with the physical processes investigated in this study as the experiments are run for a short time only (i.e., 2 Ma). Further physical and numerical parameter details are given in Table 1.

2.2. Numerical Model

Calculations are performed in two or three-dimensional Cartesian geometry with an aspect ratio of 2:1 (*x*:*z*) or 2:1:1 (*x*:*y*:*z*), respectively. This allows for efficient computation at high-resolution (e.g., 512 × 256 grid points and 100 tracers per cell; see Table 2) with a minimum grid spacing of 3 km (see supporting information Figure S1). The physical model described above is solved by the finite-difference/volume multigrid code STAGYY [e.g., *Tackley*, 2008]. Nondiffusive tracers are advected with the flow and track the composition, which is either mantle, weak crust, mantle wedge, or air.

Table 1. Control Model Parameters

Parameter	Symbol	Nondimensional Value	Dimensional Value	Unit
Reference viscosity	η_0	1	10^{23}	Pa s
Mantle depth	D	1	2890	km
Gravitational acceleration	g		9.81	ms^{-2}
Thermal conductivity	k		3	Wm^{-1} K^{-1}
Thermal diffusivity	κ	1	10^{-6}	m^2 s^{-1}
Thermal expansivity	α		3×10^{-5}	K^{-1}
Temperature gradient	ΔT	1	2500	K
Reference density	ρ_0	1	3300	kg m^{-3}
Heat capacity	Cp_0		1200	Jkg^{-1} K^{-1}
Internal heating rate	H	20	4.92×10^{-12}	Wkg^{-1}
PLASTICITY				
Friction coefficient	μ	0.25		
Cohesion	C	1577	10×10^6	Pa
Max. yield stress	$\sigma_{y,const}$	9.5×10^4	600×10^6	Pa
Ductile yield stress gradient	$\Delta\sigma_y$	0.0	0.0	
DIFFUSION CREEP				
Activation energy	E_{act}	11.55	240	kJ mol^{-1}
Activation volume	V_{act}	0.0	0	m^3 mol
STICKY-AIR LAYER				
Thickness	d_{st}	0.05	152	km
Viscosity	η_{st}	$10^{-3}\eta_0$	10^{20}	Pa s
C-condition[a]	C_{Stokes}	0.013		
WEAK CRUSTAL LAYER				
Thickness	d_{crust}	0.005	15.2	km
Viscosity	η_{crust}	η_0	10^{23}	Pa s
Friction coefficient	μ_{crust}	0.001		
Cohesion	C_{crust}	1577	10×10^6	Pa

[a]Indicates suitable free-surface approximation with sticky-air approach if

$C_{Stokes} = \frac{1}{16}\frac{\Delta\rho}{\rho_0}\left(\frac{h_{model}}{h_{st}}\right)^3\frac{\eta_{st}}{\eta_{ch}} \ll 1$, where here $\Delta\rho = 100$ kg m^{-3} is the slab-mantle density difference, $\rho_0 = 3300$ kg m^{-3} is the characteristic boundary-layer density, $h_{model} = 2890$ km is the height of the convective layer, $h_{st} = 152$ km is the height of the sticky-air layer, $\eta_{st} = 10^{20}$ Pa s is the sticky-air viscosity, and $\eta_{ch} = 10^{23}$ Pa s is the characteristic mantle viscosity [see *Crameri et al.*, 2012a].

The model domain consists of the whole mantle depth plus (for free surface cases) a "sticky-air" layer on top [*Matsumoto and Tomoda*, 1983; *Schmeling et al.*, 2008]. The sticky-air approach simulates a free surface in models calculated on an Eulerian grid, if it is applied carefully [see *Crameri et al.*, 2012a, for details and simple test conditions]: An analytic *C*-condition is necessary to test, if the applied sticky-air serves as a suitable free-surface approximation ($C \ll 1$) or not. The test condition for the sticky-air layer in the current model is fulfilled for slab-driven topographic variations with $C_{Stokes} = 0.013$ (see Table 1 for the applied formulation).

Geodynamic models with a fixed, free-slip surface cannot produce actual topography, but instead calculate a traction-derived topography ([as outlined in detail in *Crameri et al.* [2012a]). The hypothetical, vertical deflection in a free-slip model can then, however, only be accurately derived when the slope and vertical deflection of the hypothetical free surface are both small. The hypothetical vertical deflection is then

$$h = \frac{\sigma_{zz}(z=0)}{\Delta\rho_{surf}g} \qquad (10)$$

where σ_{zz} is the normal stress component at the top model boundary ($z = 0$) and $\Delta\rho_{surf}$ is the density difference between rock and air near the surface.

Table 2. Model Setups Presented in This Study

Tag	Resolution ($nx \times ny \times nz$)	Slab Dip (θ)	Radial Mantle Viscosity	Varied Physical Complexity
control	$512 \times 1 \times 256$	Variable	Isoviscous	
suite1	$512 \times 1 \times 256$	Variable	Isoviscous	Fixed (free-slip) surface
suite2	$512 \times 1 \times 256$	Variable	Isoviscous	Slab thickness
suite3	$512 \times 1 \times 256$	Variable	Isoviscous	Slab length
suite4	$512 \times 1 \times 256$	Variable	Isoviscous	Lower plate age
suite5	$512 \times 1 \times 256$	Variable	Isoviscous	Isoviscous model
suite6	$512 \times 1 \times 256$	variable	Isoviscous	Plate strength
suite7	$512 \times 1 \times 256$	Variable	Isoviscous	Upper-plate thickness
suite8	$512 \times 1 \times 256$	Variable	Viscosity jump	Mantle viscosity
suite9	$512 \times 1 \times 256$	30	Linearly increasing	Mantle viscosity
suite10	$512 \times 1 \times 256$	Variable	Isoviscous	Mantle-wedge viscosity
suite11	$512 \times 1 \times 256$	Variable	Isoviscous	Rayleigh number
suite12	$512 \times 1 \times 256$	Variable	Isoviscous	Initial bending radius
run3d	$512 \times 256 \times 256$	30	Isoviscous	
run3d$_{gap}$	$512 \times 256 \times 256$	30	Isoviscous	Lateral slab extent

In cases with steep and large surface topography (e.g., at subduction zones), it is therefore crucial to apply a true free surface or a free-surface approximation like the sticky-air approach. There are several commonly applied methods to track a freely evolving surface of the plate numerically. If the sticky-air method is used here to enable the free surface, the code StagYY tracks the composition (air or rock in this case) on Lagrangian tracers that are advected with the flow. The actual vertical subgrid position of the interface for every horizontal nodal point is then defined by a shape-function averaging of all the uppermost rock and lowermost air tracer positions. Given the high number of tracers (i.e., on average 100 tracers per cell), we are therefore able to resolve a surface topography that is vertically much more accurate than the spacing between the nodal points of our Eulerian grid.
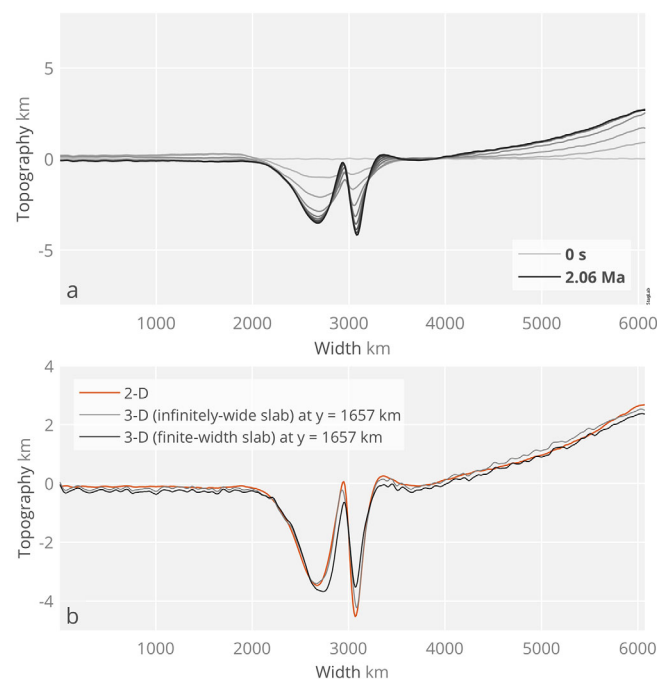
The dimensional scaling is the same as applied in *Crameri and Tackley* [2015]. *Crameri and Tackley* [2015] further provides extensive numerical and physical testing for the models applied here.

2.3. Initial Condition

In this study, we use a 2-D model geometry that allows for efficient computation and hence extended, systematical tests. Possible effects of neglecting the third spatial dimension were, however, carefully tested with two 3-D models further discussed in section 3.5.3. We find that the topography signal obtained in our 2-D model shows no significant difference to the 3-D models (see Figure 1b). In fact, the 2-D model allows us to resolve the topography more finely with a narrower tracer spacing and together with its computational efficiency makes it the optimal choice for this study.

The model assumes on-going subduction by featuring an initial finite-length slab (see supporting information Figures S2a and S2b). Additionally, an initial divergent plate boundary is assumed at the end of the subducting plate's tail and the initial boundary layer thickness w_{BL} increases away from this spreading center toward the subduction zone according to the standard $\sqrt{age}$-law

$$w_{BL}(x) = w_{BL,0} \cdot \sqrt{\Delta x_{sc}} \tag{11}$$

where $w_{BL,0}$ is a constant controlling the maximum thickness of the plate, x is the horizontal coordinate, and Δx_{sc} is the distance from the spreading center at any given position x. The radial component of the initial temperature is related to plate age as $T_z(x) = T_0 \cdot erf[(1-z)/w_{BL}(x)]$, with $T_0 = 0.64$ the initial, nondimensional mantle temperature and z the vertical coordinate ranging between 0 at the bottom to 1 at the top boundary. This leads to the initial divergent boundary (due to ridge push) that supports slab sinking at the beginning of the experiment. The upper plate has a constant thickness equal to that of the subducting plate at the trench. The plate's initial thickness is chosen to be $0.06D$ based on the observation that this is a typical boundary layer thickness with the chosen $Ra = 10^6$ and $H = 20$ [see *Crameri and Tackley*, 2015]. This then leads to a characteristic plate thickness defined by the 1700 K isotherm of $d_{p0} = 93$ km in the control model.

Figure 1. Surface topography of the model. (a) Short-term temporal topography evolution from a flat initial surface to the (slowly-changing) free-surface equilibrium over 2 Ma in 250 ka intervals in the *control* model. (b) Comparison of the surface topography between the *control* 2-D model (red line) and two corresponding 3-D models with either an initial, infinitely wide slab corresponding to the 2-D model (*run3d*; grey line) or an initial finite width slab (*run3d_{gap}*; black line).

The initially 700 km long, straight slab (from trench to slab tip) is inclined to the surface plate by a certain angle, θ, through an abrupt kink, which relaxes during model evolution. The plate bending radius therefore evolves naturally until the 2 Ma state. The slab has an initially constant thickness corresponding to the surface plate thickness at the trench. This is done by applying the same temperature profile as for the surface plate but normal to the slab's inclined surface, which also allows to change the slab's thickness separately from everything else. In nature, the slab-dip angle strongly varies with depth (slabs are often bent) but also along the strike of a subduction zone. Hence, it is difficult to characterize a subduction zone with just one single value of slab-dip angle. It is, however, more straightforward to define a dip angle in our simplified model thanks to the two-dimensional setup and the straight geometry of the initial slab. Here, the slab-dip angle, θ, is defined as an initial condition at the shallow depth range of around $150-250$ km. Subsequently during its free evolution, it is measured at a depth of 175 km (see section 2.6.3 for more details). In this study, the initial shallow-depth slab dip is varied between 20 and 60°. Given the initially straight nature of the model slab, shallower or steeper dips are not feasible due to unnatural coupling with the upper plate and an unnatural strong bending (i.e., kink) of the plate, respectively.

All experiments start with an initially flat surface and are then run for more than a hundred time steps over a model time period of 2 Ma to reach a slowly changing free-surface topography equilibrium before they are investigated (see supporting information Figure S2); The free surface equilibrium is generally reached after <1 Ma (see Figure 1a). The adjustment period of 2 Ma allows the model to adjust self-consistently (e.g., full isostatic surface adjustments, minor adjustments toward more natural slab bending radius and less sharp local temperature contrasts) and so, to minimize possible artificial impacts from the initial condition. It is worth mentioning that using a more nature-like Ra-number of around 10^7 would mean a corresponding adjustment time of only 0.2 Ma. The following, longer evolution of the model is therefore additionally considered and discussed in section 3.2. This adjustment period of 2 Ma model evolution is important: It is neither too short nor too long to systematically study the quasi steady state surface topography of variable model setups in the framework of the largely unaltered (and hence comparable) thermal initial condition.

2.4. Topography Indication Points

The resulting topography above an asymmetric, single-sided subduction zone including a weak subduction fault is asymmetric and characterized by distinct topographic features that are unique to either the subducting or the overriding plate. These characteristic topographic indication points and their specific measurement are indicated in Figure 2 and explained in Table 3. Figure 3d shows the location of these characteristics in the simplified, long-wavelength surface topography of a convergent boundary obtained in our reference model. In the direction from the subducting to the overriding plate these are as listed below.

1. The viscous fore-bulge (or outer rise) is the positive deflection in front of the collision zone. It is the transient, viscous uplift outboard of the trench caused by the downward bending of the subducting plate
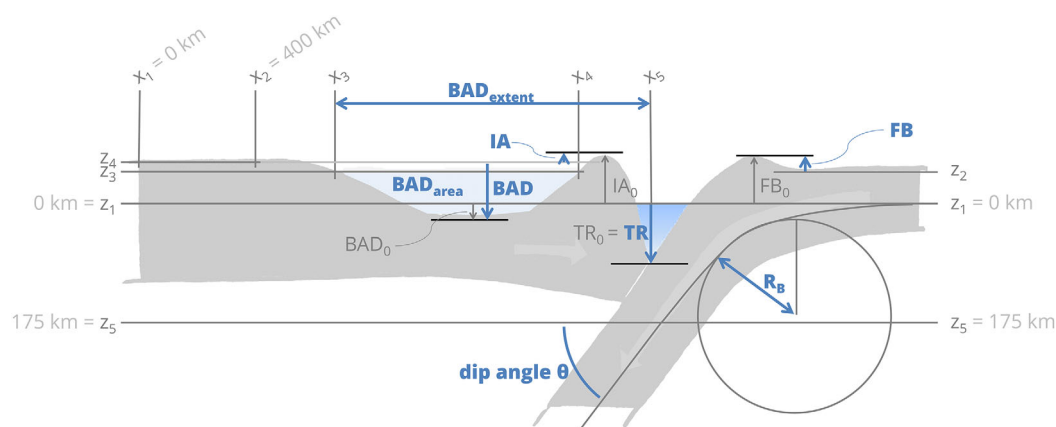
Figure 2. Deriving the topographic characteristics at a subduction zone, which are from the subducting plate (right) toward the overriding plate (left) viscous fore-bulge (FB), subduction trench (TR), island-arc (IA), and back-arc depression (BAD). The shallow-depth slab dip, θ, is taken at the depth z_5, the bending radius R_B is derived by fitting a circle to the point of maximal plate bending. See text and Table 3 for more details.
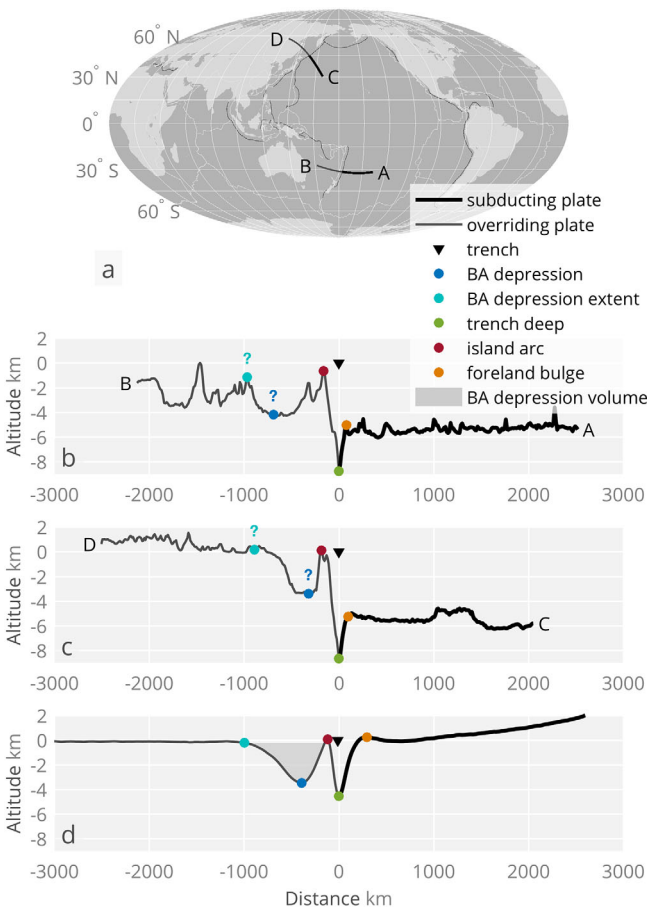
Table 3. Characteristic Topographic Points

Geometric Characteristic	Abbreviation	Measurement Method[a,c]
Viscous Fore-Bulge	FB	$FB = FB_0 - z_2$
Subduction Trench	TR	$TR = TR_0$
Island-Arc	IA	$IA = IA_0 - z_4$
Back-Arc Depression Depth	BAD	$BAD = BAD_0 - z_4$
Back-Arc Depression Extent	BAD_{extent}	$BAD_{extent} = x_{TR} - x_3$
Back-Arc Depression Area	BAD_{area}	$BAD_{area} = \int_{x_3}^{x_4} z_3 - z(x)\, dx$

[a] $x_1 = 0$, $x_2 = 400$ km, $x_3 = x(z = z_3)$, and $x_4 = x_{TR}$.
[b] $z_1 = 0$ km is the sea level, $z_2 = z_{min}(x > x_{FB})$, $z_4 = z_{mean}(x < x_2)$, and $z_3 = z_4 - 2(z_{max} - z_{min})$ for $x < x_2$.
[c] See graphical representation in Figure 2.

that floats on a low-viscosity mantle [*de Bremaecker*, 1977]. The fore-bulge height is here defined as the difference between the maximum height of the flexural bulge (FB_0) and the minimum plate-surface height at its side further away from the subduction zone (z_2).

interface at Earth's surface between upper and lower plate. It is probably of a dynamic origin and influenced by many factors [*Zhong and Gurnis*, 1994]. The trench depth is here defined by the minimum of the negative deflection (TR_0) relative to the sea level ($z_1 = 0$ km) of the model.

2. The subduction trench is the depression above the collision zone and therefore indicates the

3. The island-arc (or volcanic arc) is the collisional high that is caused by the compression due to (ocean-ocean) plate convergence. Apart from its dynamic origin, it can be strongly affected by volcanism [*Karig*, 1971]. It is here defined by the maximum of the positive deflection (IA_0) relative to the mean upper plate height level on the leftmost 400 km of the model (z_4).

4. The back-arc depression (or basin) is the down-ward deflection of the upper plate further away from the trench. The deflection is mainly caused by upper plate extension, or even spreading [*Karig*, 1971], due to subduction-trench retreat and the dynamic coupling with the sinking slab below. The back-arc depression depth is here given as the maximum depression on the upper plate (BAD_0) relative to the mean upper plate height level on the leftmost 400 km of the model (z_4). This is necessary due to the different isostatic compensation between different models (e.g., with variable upper plate thicknesses), which leads to differently elevated upper plates.

Figure 3. Surface topography across convergent plate boundaries and characteristic topography indication points (colored dots). (a) Map indicating the orientation of the observational profiles. The profiles show (b) the observational topography after *Ryan et al.* [2009] and *Amante and Eakins* [2009] across the Kamchatka and (c) the Kermadec subduction zones, and (d) the modeled topography of the *control* model. Black line segments indicate the subducting and grey line segments indicate the overriding plate portion.

In addition to these four topographic points, two additional measures are taken and discussed here. First, a measure is taken for the maximum horizontal extent of the back-arc depression away from the trench (BAD_{extent}). It is here defined by the distance between the trench (x_5) and the highest surface point of the back-arc deflection away from (and measured from) the trench (x_3) that still is lower than twice the maximum vertical variation occurring in the 400 km-wide reference upper-plate portion (z_3). Second, the volume of the back-arc depression, which, in 2-D models,

corresponds to a vertical area, is measured here. The basin's horizontal extent is limited by the point of maximum basin extent (x_3) and the point on the same level toward the island-arc height (x_4). In the vertical direction, it is limited by the undeflected mean height of the upper plate and its maximum depth.

The vertical amplitude of the characteristic topographic points is later given in percentage of the characteristic plate thickness ($\%_{cpt}$), which is here $d_{p0} = 93$ km (i.e., the thermal-lithosphere thickness at 1700 K in the control model), to allow scaling (e.g., to systems with a different Rayleigh number and thus different plate thicknesses).

2.5. Subduction Parameters

Our investigation includes numerous subduction parameters and focusses on their specific impact on each of the four surface-topography characteristics. The subduction parameters that are predefined as initial condition and tested here are categorized into three groups:

1. Buoyancy Parameters including slab thickness and slab length,
2. Rheological Parameters including plate strength, radial mantle viscosity, mantle-wedge viscosity and slab-mantle viscosity contrast,
3. Geometric Parameters including slab-dip angle, plate bending, slab length, and three-dimensionality.

Other important subduction parameters affecting our model like subduction-channel strength, plate-mantle viscosity contrast, or mantle-viscosity reduction due to melting have been extensively studied in *Crameri and Tackley* [2015] and are not further discussed here.

2.6. Diagnostics

More than a hundred experiments are carried out for this study. To ensure efficient postprocessing of all model data, various fully automated diagnostics are applied during postprocessing using StagLab (www.fabiocrameri.ch/software) and explained in detail below.

2.6.1. Topography Components

Surface topography is often split into individual components in order to better separate the various and very diverse contributions. Here, we consider two different components of topography: The *isostatic* component and the remaining, nonisostatic, *residual* component.

The *isostatic* topography component can be calculated using the base of the plate (i.e., here the 1700 K isotherm) as the compensation depth (see supporting information Figure S3). Depending on whether the plate is denser or lighter than the mantle, the isostatic topography component for each vertical column along the lateral model extent is given by

$$z_{topo,iso}(\rho_p) = \begin{cases} \dfrac{(\rho_m - \rho_p)d_{LAB}}{\rho_p - \rho_{air}}, & \text{if } \rho_p \leq \rho_m \\[2mm] \dfrac{(\rho_m - \rho_p)d_p}{\rho_m - \rho_{air}}, & \text{if } \rho_p > \rho_m \end{cases} \tag{12}$$

where ρ_p is the vertically averaged density of the plate at each horizontal point in space, ρ_m is the horizontal mean density of the upper mantle below the plate away from the sinking slab, ρ_{air} is the density of the air (i.e., the sticky air, if applied), d_{LAB} is the variable depth of the thermal lithosphere-asthenosphere boundary (LAB) defined by the 1700 K isotherm at each horizontal point in space, and d_p is the variable plate thickness at each horizontal point in space including surface topography (i.e., the thickness between the rock-air interface and the 1700 K isotherm).

The resulting isostatic topography component throughout the model is then normalized to produce a mean value that corresponds to the sea level according to

$$z_{topo,iso,0}(x) = z_{topo,iso}(x) - \langle z_{topo,iso} \rangle \tag{13}$$

where $\langle z_{topo,iso} \rangle$ is the mean of the model-wide isostatic topography component and x is the horizontal coordinate. This is needed to account for both the conservation of volume in our model given an incompressible mantle and the coherence of the plate at the surface.

The resulting, *residual* topography component is then simply given by

$$z_{topo,res} = z_{topo,total} - z_{topo,iso,0}$$ (14)

where $z_{topo,total}$ is the surface topography of the model. We consider the residual topography component as that part of topography that cannot be explained by the isostatic dynamics of the plate. Instead, it can, for example, be caused by horizontal tectonic forces from within the plate itself, or by dynamic forces from within the convecting mantle below.

2.6.2. Slab-Mantle Viscosity Contrast

The slab-mantle viscosity contrast, $\Delta\eta_{LA}$, is used in this study to characterize our experiments with different rheology. It is here defined as the difference between the slab's yield viscosity, $\eta_{y,slab}$, and the mean viscosity of the upper mantle (without sinking plate portions).

2.6.3. Shallow-Depth Slab Dip

The shallow-depth slab dip is prescribed initially (see section 2.3) but then evolves freely. STAGLAB provides an automated detection of the shallow-depth slab dip that enables tracking it throughout the model evolution (see e.g., section 3.2). The shallow-depth slab dip angle, θ, is here measured in between the two depth levels $z_{5A} = 1.25d_p$ and $z_{5B} = 7/4z_2$, where d_p is the current mean lithosphere thickness away from the subduction zone (see Figure 2). The measuring depth for the slab-dip angle is therefore located below the lithosphere and given by

$$z_5 = z_{5A} + \frac{z_{5B} - z_{5A}}{2} = 175 \ km$$ (15)

as indicated in Figure 2.

2.6.4. Plate Bending

The minimum-bending radius, R_B, is yet another useful diagnostic tool. After being prescribed with the initial condition, it is evolving freely but fully automatically tracked during the subsequent model evolution in a postprocessing step with STAGLAB. It is derived by applying the spline method, similar to the one outlined in *Petersen et al.* [2016], except that STAGLAB uses temperature contours to derive the subducting plate geometry. The curvature, R_{curv}, of the line representing the plate geometry at every point over its whole width is given by

$$R_{curv}(x) = \frac{[1 + (\frac{dz}{dx})^2]^{3/2}}{|\frac{d^2z}{dx^2}|}$$ (16)

where dx and dy are the incremental spatial change of the line at the horizontal location, x, in x and z direction, respectively. The minimum plate-bending radius (i.e., maximum bending) at the kink of the subduction zone, R_B, corresponds then simply to the minimum value of curvature, R_{curv}, found along the considered plate portion and thus given by

$$R_B = \min[R_{curv}].$$ (17)

2.6.5. Viscous Bending Dissipation

Finally, the viscous dissipation in the lithosphere produced by plate bending at the subduction zone is calculated within STAGLAB. An approximation for the viscous bending dissipation is given in *Conrad and Hager* [1999] for a purely viscous plate. With the additions outlined in *Buffett* [2006], the viscous dissipation for a viscoplastic plate is given by

$$\phi_L^{vd} = C_l v_p \sigma_{y,p} \left(\frac{d_s^2}{R_B} \right)$$ (18)

where $C_l = 1/6$ is a constant, v_p is the lower-plate velocity, d_s is the slab thickness, and $\sigma_{y,p}$ is the maximum yield stress inside the bending portion of the plate. Here, we normalize the lithospheric bending dissipation ϕ_L^{vd} with $\phi_{L,char}^{vd} = 874$ W/m, the value derived in the control model with a slab that dips at 30° using

$$\phi_{L,norm}^{vd} = \frac{\phi_L^{vd}}{\phi_{L,char}^{vd}}.$$ (19)

The predicted value from equation (18) is in good agreement to the viscous dissipation calculated in the model directly ($\phi_{vd} = \sigma\dot{\varepsilon}A_{cell}$, where A_{cell} is the corresponding grid-cell area) when integrating over the surface plate and bending area, but neglecting the subduction channel (see supporting information Figure S4).

3. Results

3.1. Boundary Conditions

Surface topography has been shown to be a key player even for large-scale mantle dynamics: It is, for example, a necessity to produce nature-like single-sided subduction [*Crameri et al.*, 2012b]. Yet, most mantle convection models still use a vertically fixed, free-slip surface due to numerical simplification. Here, we compare therefore the surface topography, calculated via the normal stress created at the fixed and flat top model boundary, with the actual topography of a free surface similar to for example, *Gurnis et al.* [1996]. The calculated surface deflection in the free-slip models is representing a fictive topography corresponding to the normal stresses occurring at the top model boundary (see section 2.2). As such, it has three nonnegligible drawbacks when modeling a subduction zone:

1. The traction-derived topography is only justified for small slopes ($\ll 1$) and low amplitudes ($h_{topo}/D \ll 1$, where D is the depth of the model) [*Crameri et al.*, 2012a].
2. The traction-derived topography is only justified, if there are small lateral viscosity variations near the surface. Large lateral viscosity variations near the surface might deteriorate the pressure and hence the topography [*King*, 2009].
3. The traction-derived topography is always instantaneous. It does therefore not capture the natural delay between the occurrence of stress and the actual uplift. The gradual isostatic adjustment of an isostatically uncompensated plate deflection (as might occur in a modeling sense due to an artificial initial condition or, in nature, due to a fast process like melting of an ice sheet) can, for example, not be captured with a free-slip surface [*Crameri et al.*, 2012a]. It might, however, not be that important to resolve such short-term elevation changes better when modeling long-term mantle convection.

Although previous studies seem to have applied it successfully (i.e., without using a weak crustal layer and a model that produces self-consistent single-sided subduction), our high-resolution results for a free-slip surface indicate that the computed, traction-derived topography is, after all, strongly influenced by unnatural normal stresses occurring at the vertically fixed top boundary close to a convergent boundary (Figure 4 and supporting information Figure S5). The traction-derived topography in our free-slip experiments cannot reproduce the free-surface result, even though the isostatic component of topography is similar between the two model setups (see Figures 4a and 4d). Apart from the missing plate-bending stresses when applying a vertically fixed surface [see *Thielmann et al.*, 2015], this must be the result of the high lateral viscosity variations of our model (between strong intact and weak yielding zones of the crustal layer, and between weak subduction channel and strong plate interior), and unnatural plate bending at the subduction trench: As the plate approaches the subduction trench, it is forced to stay flat (due to the fixed surface) instead of creating a fore-bulge, which would reduce the bending radius of the plate. The direct result of that fixation is that the subducting plate bends more strongly at the collision zone and thereby creates artificial stresses within but also on top of the plate as has been shown previously [*Crameri and Tackley*, 2016]. These artificial normal stresses at the model top boundary cause, for example, yielding in the weak crustal layer on top of the subducting plate close to the trench, but also at shallow depth on the upper plate, which does not have weak crust on top (see Figure 4e). These artificial stresses then add another artificial component to the resulting surface topography. In summary, the topography in our high-resolution, free-slip surface models does not reproduce the characteristic topographic signal as observed in the free surface models and in nature (Figure 3). In the remainder of this study, we use therefore a model incorporating a free top surface.

3.2. Time Evolution

Although most of the results we present from this model are taken at an early stage of model evolution (see section 2.3), it is important to first clarify how the model behaves on a longer-time scale. Figure 5 presents the long-term evolution of the model. Here, the side boundaries are periodic instead of free-slip to prevent unnatural forcing during its longer evolution. As the slab sinks deeper, slab pull and slab suction increase. This leads to both a gradual speedup of the subducting plate and an increased convergence rate. The much faster subducting plate also leads to an increase in lithospheric bending dissipation, which does more than double between the first and last snapshot shown in Figure 5. Another result of the steadily growing slab volume is a deeper and more voluminous back-arc depression at later stages of the model evolution.
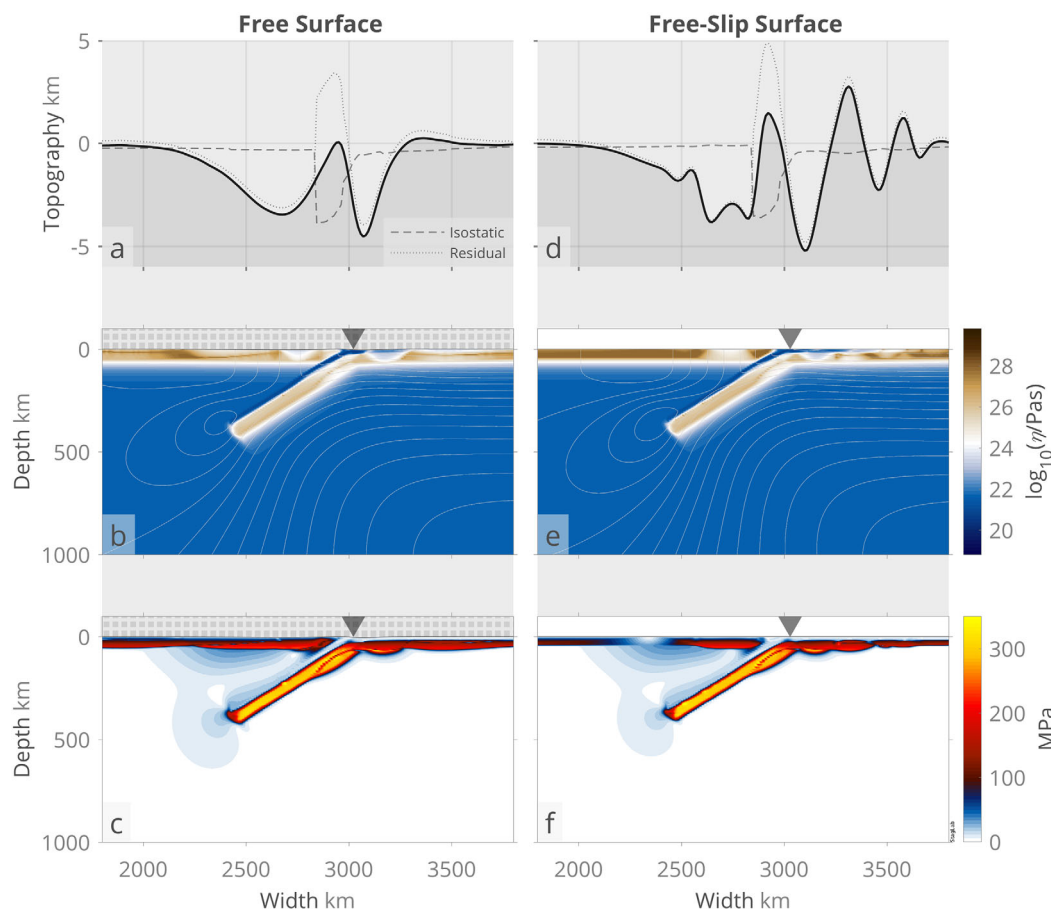
Figure 4. Comparison between applying (a, b, c) a realistic free top surface (the sticky-air layer is removed visually and filled with a hatched grey area) in the *control* model and (d, e, f) a commonly used vertically fixed (i.e., free-slip) top surface of the *suite*1 model. Shown are close-ups of the (a) observed and (d) calculated (traction-derived) topography including isostatic and residual components, the effective viscosity (middle row), and the second invariant of the stress tensor (bottom row). The grey contours indicate flow direction.

Even after a long-time period, the initially at 30°-dipping shallow slab dips at 32°, indicating it to be the system's natural shallow-depth slab dip. Observations at Earth's subduction zones indicate the exact same mean shallow-depth slab dip of 32° but include a significant amount of ocean-continent subduction zones, which tend to cause shallower slabs [*Lallemand et al.*, 2005].

3.3. Buoyancy Parameters

There are various buoyancy, or in other words, driving forces in a subduction system that strongly control surface topography. These are in particular slab pull and slab suction, the two dominating dynamic forces in Earth's mantle. In Figure 6, we present a cumulation of our experimental data to generalize the effect a variable slab buoyancy has on surface topography: A more negatively buoyant slab clearly accentuates the regional highs and lows of the plate surface. The topographic impact of the most important buoyancy parameters in our model that drive subduction, which are slab thickness and slab length, are mentioned below.

3.3.1. Slab Thickness and Length

First, we test here the specific topographic effects of slab buoyancy by varying the initial slab thickness. Only varying the slab thickness, while keeping the plate thickness at the surface and all other parameters unchanged, allows us to extract the topographic impact specifically linked to slab-buoyancy variation. Thicker slabs vary from the control setup in such a way, that the coldest portion of the slab is widened. This method allows for a controlled variation of slab buoyancy and does not impact the plate strength in the bending area: Ongoing plate subduction during the initial model adjustment time of 2 Ma delivers unaltered plate portions to the bending area.
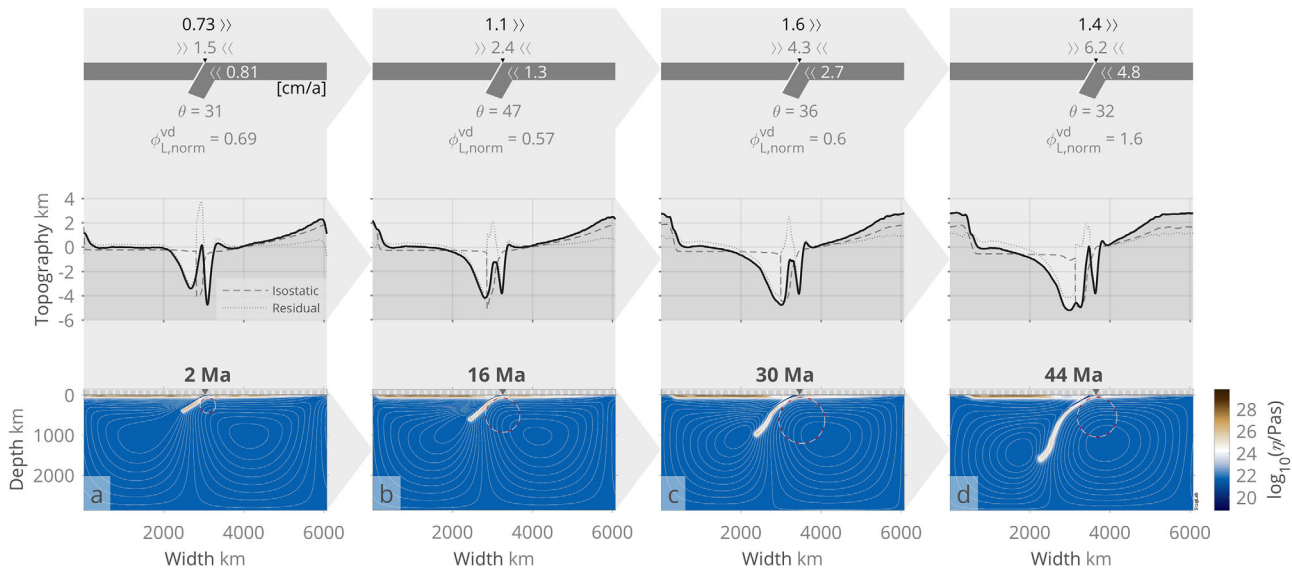
Figure 5. Time evolution (from left to right) of the *control* model with an initial shallow-depth slab dip of 30°. Shown are, in the top row, tectonic parameters including current trench, convergence, and plate velocities, as well as shallow-depth slab-dip angle (θ) and relative bending dissipation ($\phi_{L,norm}^{vd}$). The middle row shows surface topography with isostatic and residual components, and the bottom row shows effective viscosity with grey contours indicating flow direction. Dark triangles indicate subduction trench location and red-white-dashed circles indicate minimum plate bending radius, R_B (ranging from 292 km at 2 Ma to 573 km at 30 Ma and back down to 494 km at 44 Ma).

Our systematic test highlights the generally linear interaction between the variation in slab buoyancy and the resulting deflection for each characteristic topographic point (see supporting information Figure S6). According to the linear interpolations of our results (corresponding scaling laws are given in supporting information Figure S6), an increase in thickness of one characteristic plate thickness (i.e., 100%$_{cpt}$) of the 700 km long slab causes a more negatively buoyant slab and hence an increase in fore-bulge height of
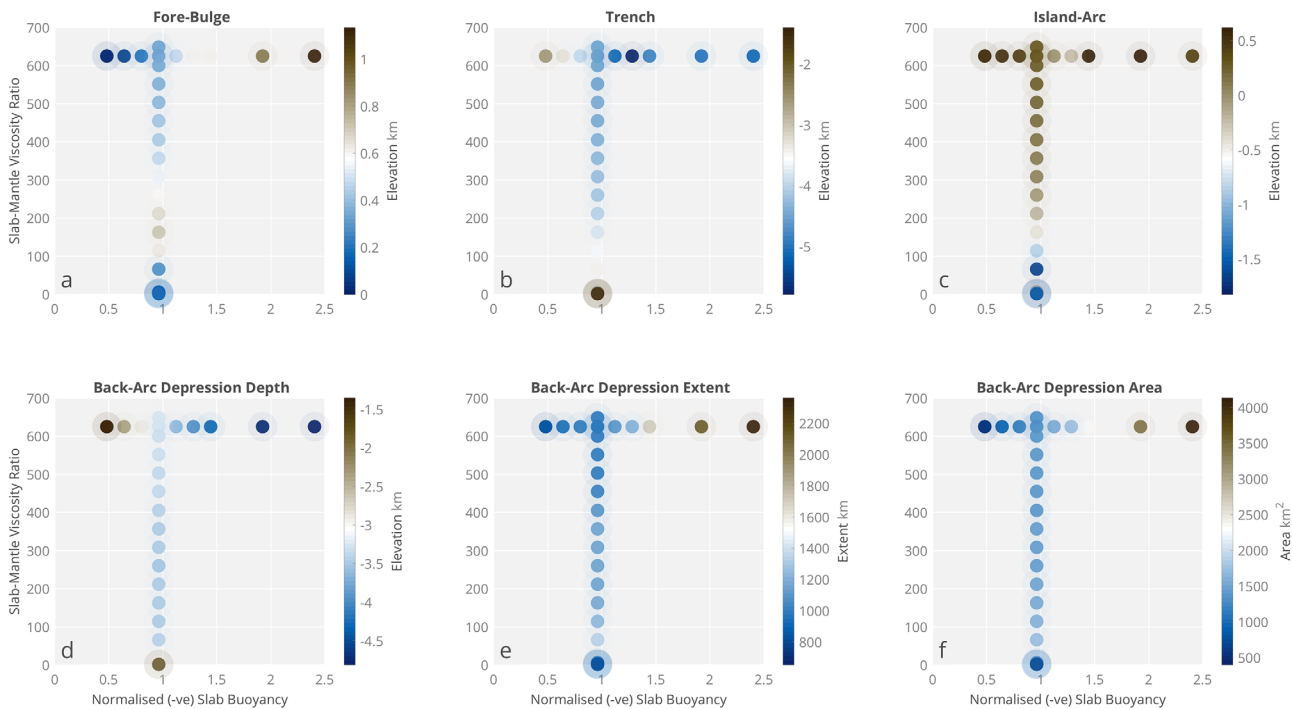
Figure 6. Effect of both slab buoyancy (the higher the value, the more negatively buoyant the slab) and rheology (i.e., slab-mantle viscosity ratio) on regional topographic features: (a) Fore-bulge height, (b) trench depth, (c) island-arc height, (d) back-arc depression depth, (e) horizontal back-arc depression extent, and (f) total deflected area of the back-arc depression. Colors indicate surface elevation and the degree of shading in the big circles indicates multiple data points.

around 0.72%$_{cpt}$ (i.e., 0.67 km), an increase in trench depth of around 3.2%$_{cpt}$ (i.e., 2.98 km), a decrease in island-arc height of around 1.2%$_{cpt}$ (i.e., 1.12 km), an increase in back-arc depression depth of around 2.1%$_{cpt}$ (i.e., 1.96 km), an increase in back-arc depression width of around 311%$_{cpt}$ (i.e., 290 km), and an increase in total back-arc depression area of around 13%$_{cpt^2}$ (i.e., 1130 km^2).

The total slab buoyancy not only depends, however, on the slab's thickness (i.e., its age), but also on its length (i.e., the subduction zone's history). Having quantified the linear topographic effect of varying the slab's weight (i.e., slab buoyancy) on each of the surface-topography features (e.g., the forcing of a 700 km long slab portion, with a standard thickness given in the control model, deepens the trench by ∼3 km), we can now extract the (additional) buoyancy signal that goes along with a longer or shorter slab (compared to the control model with a 700 km long slab). A 1400 km long slab deepens, for example, the trench by ∼3 km compared to the control model given that is has a constant thickness (which is the case in our model). This is due to the additional 700 km of slab that additionally pull down the trench compared to the control model. Considering only the variation in slab buoyancy depending on the variation of its length, the topographic effect is in accordance to the results above, as it is only depending on the total weight of the slab: A shorter and thus lighter slab decreases the overall amplitude of the topographic signals at the surface (see supporting information Figure S7). Slab buoyancy is thus, whether controlled by slab thickness or length, a key controlling factor for the amplitude of convection-induced topography.

3.4. Rheological Parameters

There are various rheological, or in other words, resisting forces in a subduction system that strongly control surface topography. The graphical cumulation of experimental data in Figure 6 also highlights the general topographic impact of rheology, expressed in slab-mantle viscosity contrast. A higher viscosity gradient generally leads to accentuation of the topographic highs and lows at the plate surface. The topographic impact of the specific important rheological parameters that resist subduction like the presence of a stiff top boundary layer, its strength, and the viscosity of the mantle and mantle wedge are mentioned below.

3.4.1. Plate Strength

The most simplified model we discuss here ignores the presence of a stiff, upper boundary layer (i.e., a surface plate). In this model, all the rocky material is isoviscous, ignoring the temperature and pressure-dependence of viscosity. Differences in viscosity occur only in the low-viscosity air layer or in regions of the mantle that are under small confining pressure and high stress and thus yield (e.g., the subduction fault). The comparison to these isoviscous experiments, shown in supporting information Figures S8 and S9, allows us to investigate the impact a high-viscosity surface plate has on the transmission of convective stresses from the mantle to the surface. Key features distinguishing the isoviscous model from the control model with a high-viscosity plate are a more symmetric surface depression that laterally aligns approximately with the lateral extent of the shallow slab, no viscous fore-bulge and a shallower trench (supporting information Figure S9). This impossibility of reproducing characteristic regional subduction-zone topography without lateral viscosity variations has been pointed out already previously [e.g., *Kaban et al.*, 2014; *Gérault et al.*, 2015].

Additionally, we have varied plate strength in an additional suite of variable-viscosity experiments (supporting information Figure S10) and derived scaling laws, which are given in supporting information Figure S11. We present the results in terms of a mean yield strength of the plate, $\sigma_{y,mean}$ (see equation (9)). Compared to other physical aspects, the topographic impact of plate strength seems to be minor, but by no means negligible. A variable plate strength impacts the height of the viscous fore-bulge that decreases and becomes smoother for stronger plates. The exception is very weak plates with a mean strength of $\sigma_{y,mean}$ < 100 MPa, where there is little or no fore-bulge visible at all due to the increased internal deformation (supporting information Figures S10a and S11a). With increasing plate strength, the depth of the trench in the control model converges exponentially toward a maximum depth of 4.62 km (i.e., $0.049 d_{p0}$; supporting information Figure S11b). Similarly, we find that the island-arc height (*IAH*) can be described as an exponential function of plate strength (*PS*) approaching a maximum height of IAH_o = 285 m with respect to the upper plate. Apart from the uncorrelated depth in very weak plates with a mean strength of $\sigma_{y,mean}$ < 200 MPa, there is a linear decrease of the back-arc depression toward stronger plates (supporting information Figure S11d). The shallowing of the basin is of the order of 120 m per 100 MPa strength increase and can be explained by the plate's resistance to bending, which depends on its strength. The back-arc depression's horizontal extent strongly increases for very weak plates (i.e., $\sigma_{y,mean}$ < 270 MPa), but is nearly constant at a

maximum distance of 1000 km away from the trench for stronger plates (supporting information Figure S11e). Combining these two changes in basin width and depth, the total resulting area of the back-arc depression is therefore also nearly stable for plates with a mean strength of $\sigma_{y,mean} > 270$ MPa (supporting information Figure S11f).

We find the same qualitative behavior when only varying the upper plate thickness (see supporting information Figure S12) and hence its strength and natural bending radius (see section 2.6.4): For a thicker upper plate, we find, after correcting its subsidence with respect to the lighter lower plate, a strongly amplified fore-bulge (especially for steeper dipping slabs; see section 3.5.2) and island-arc height, and a reduced back-arc depression that is additionally positioned further away from the trench. On the contrary, there is only a minor amplification of trench depth with a thicker upper plate.

A younger subducting plate (e.g., a factor of 2/3 thinner; supporting information Figure S13) on the other hand not only means that the slab is less heavy (as discussed previously), but also that the lower plate is easier to bend and produces less viscous bending dissipation (supporting information Figure S14). The thinner lower plate causes a significantly shallower fore-bulge, trench, and back-arc depression, especially for steeply dipping slabs when the resisting forces play a more important role (see section 3.5.2).

3.4.2. Radial Mantle Viscosity

The viscosity of the slab's surrounding medium is a crucial component in the subduction system and has also a strong control on subduction-related surface topography. A high-viscosity lower mantle (e.g., a factor of 30 larger than the upper mantle) is, for example, believed to play an important part in reducing the observed, long-wavelength geoid highs [Hager, 1984]. Three different radial mantle-viscosity profiles are therefore tested here to distinguish the effect of the surrounding mantle on the resulting topography. In the three different experiments, the mantle is either (i) isoviscous, (ii) has an exponentially increasing viscosity with depth using a variable activation volume V_{act} (see equation (5)), or (iii) has a viscosity jump at the upper mantle-lower mantle transition zone of a factor 100, characterizing an upper bound within the uncertainty of radial mantle viscosity (Figure 7).
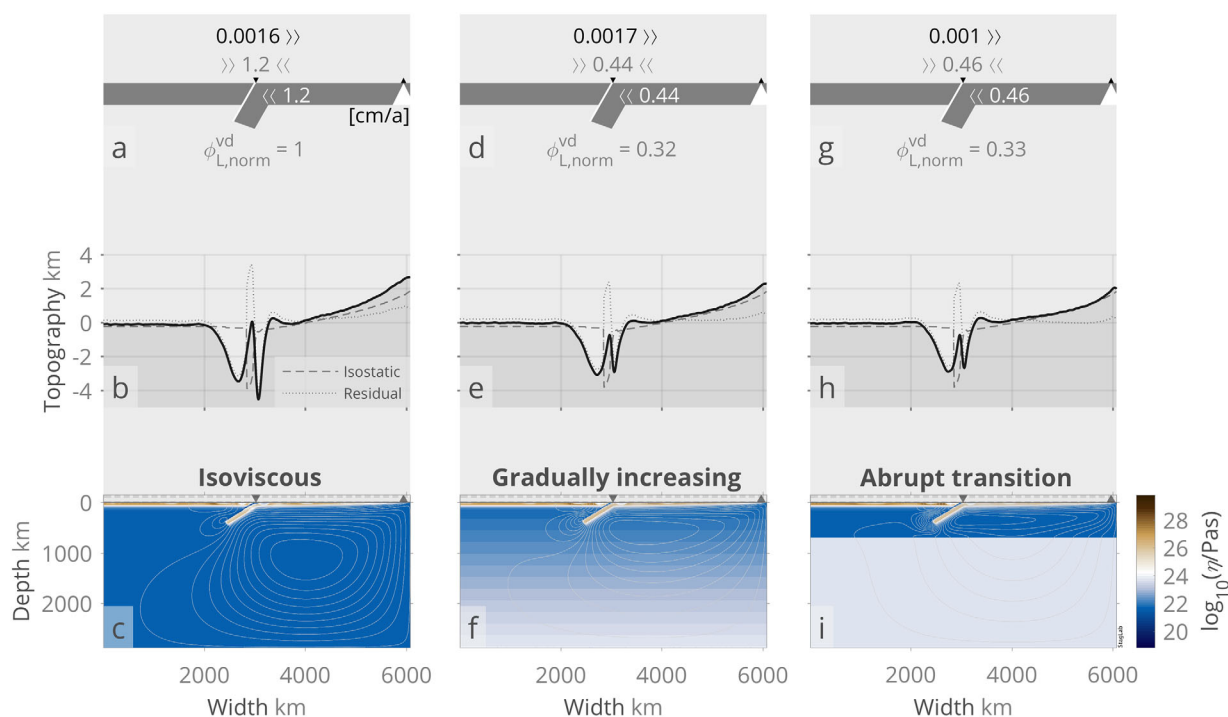
Figure 7. Experiments highlighting the effect of differences in radial mantle viscosity that is either (a, b, c) isoviscous (control model), (d, e, f) radially increasing with depth using $V_{act} = 8.5 \times 10^{-7}$ m^3/mol (suite9 model), or (g, h, i) has a viscosity jump of factor $\Delta \eta = 100$ at 600 km depth (suite8 model). Shown are, in the top row, tectonic parameters including current trench, convergence, and plate velocities (given in cm/a), as well as relative bending dissipation ($\phi_{L,norm}^{vd}$). The middle row shows surface topography with isostatic and residual components, and the bottom row effective viscosity with grey contours indicating instantaneous mantle flow.

One main physical complexity characterizes the difference observed in these three experiments: The increased resistance for the slab to sink for any added radial viscosity increase (exponentially with depth or as an abrupt transition). The higher the viscosity increase in the mantle below and around the sinking slab, the more work is needed for deformation: Large amounts of the total slab buoyancy force are converted into deformation of the mantle below the slab rather than used for pulling the plate downward. The subduction-induced flow cell consequently decreases in spatial extent and localizes to the uppermost part of the mantle. Additionally, slab pull is counteracted by a higher slab-sinking resistance within the mantle, which then also reduces the overall amplitudes in the observed topographic signal.

In addition to the comparison between these three model setups, we study the impact of a radially increasing mantle viscosity more systematically: We conduct a suite of experiments for which we vary the activation volume, V_{act} (supporting information Figures S15 and S16), and with that also the slab-mantle viscosity contrast, $\Delta\eta_{LA}$ (Figure 6). For a high V_{act} (i.e., a lower $\Delta\eta_{LA}$) and hence strong resistance to slab sinking, we observe a slightly less elevated fore-bulge, a shallower trench depression, a less-elevated island arc, and a shallower back-arc depression. There is no clear correlation between mantle viscosity gradient and horizontal extent or area of the back-arc-basin.

3.4.3. Low-Viscosity Mantle Wedge

The mantle wedge is believed to have a lower viscosity by at least an order of magnitude compared to the rest of the upper mantle due to the presence of volatiles released by the sinking plate [*Hirth and Kohlstedt*, 1996]. It is further believed to have an important impact on the surface deflection above [*Billen and Gurnis*, 2001; *Billen et al.*, 2003; *Gérault et al.*, 2015]. We tested therefore additionally a suite of experiments using a model with a low-viscosity (i.e., two-orders of magnitude lower) mantle wedge (supporting information Figure S17). To do this, the viscosity between the slab top and the base of the upper plate (i.e., the 750 K isotherm) is reduced by a factor of 100.

Once a low-viscosity mantle wedge is present, we observe smaller amplitudes in the topography on the upper plate, but also a deeper trench and a slightly more pronounced viscous fore-bulge (see Figure 8). The first observation is mainly caused by the decoupling effect of a low-viscosity region between slab and upper plate, as is highlighted by increased deformation rates in the wedge (see Figures 8c and 8f). The latter two observations are caused by less slab-sinking resistance due to the lower viscosity material present on the top of the slab.

3.5. Geometric Parameters

There are various geometric aspects in a subduction system that strongly control surface topography. The topographic impact of the most important geometric parameters that impact subduction, which are slab length, shallow-depth slab dip angle and 3-D flow, are mentioned below.

3.5.1. Slab Length

Slab length varies strongly in nature between different subduction zones and through time and might have an important impact on surface topography through, for example, slab anchoring in the lower mantle [see e.g., *Gérault et al.*, 2015]. Here, the purely geometric aspect of a variable slab length (neglecting a possible interaction with the upper mantle transition zone) is tested. The topographic effect of variable slab buoyancy has been quantified in section 3.3.1. We can therefore remove the part of the topographic signal that is solely caused by a difference in slab buoyancy associated with different slab length. We make, for example, the resulting trench depression shallower by ∼3 km in the experiment with a 1400 km long slab. This is to account for the additional 700 km of slab that additionally pull down the trench compared to the control model. The remaining topographic signal describes then the actual surface deflection that is solely caused by the geometric variation of the slab (i.e., longer or shorter) and neglects the effect of the variation in the total slab weight.

A suite of experiments with varying slab length (e.g., supporting information Figure S7) indicates that the viscous fore-bulge height is fully independent on the geometric aspect of slab length (supporting information Figure S18a). In contrast, a significant decrease of trench depth due to the geometric effect of longer slabs is observable (supporting information Figure S18b). This indicates that, after removing the dominating effect of the slab-buoyancy force, the other, resisting forces become dominating for longer slabs: Resisting forces (e.g., friction) increase along longer slabs as there is more surface area, counteract the slab pull and therefore reduce the net forcing the slab produces at the surface. The island-arc height increases (mostly)
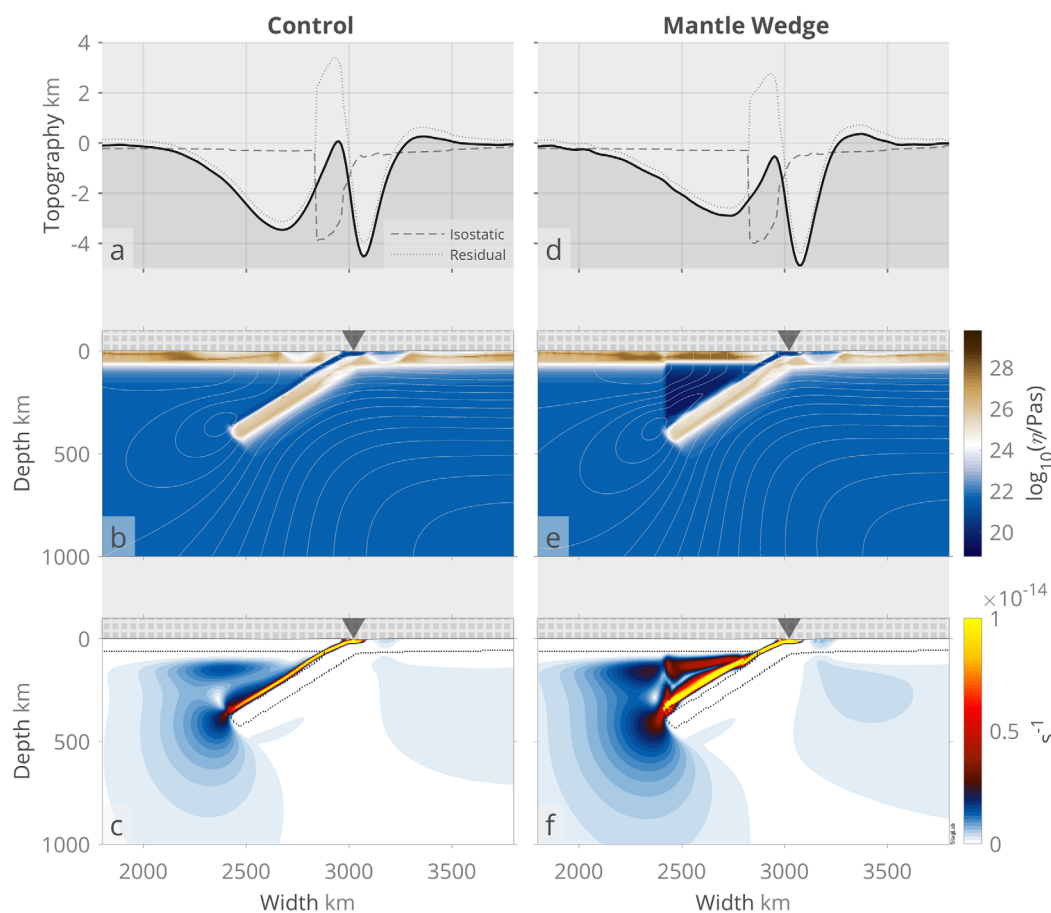
Figure 8. The effect of a low-viscosity mantle wedge highlighted by the comparison between (a–c) the *control* model and (d–f) the *suite*10 model with a 100 times lower viscosity in the mantle wedge. Shown are surface topography with (top row) isostatic and residual components, (middle row) effective viscosity with grey contours indicating instantaneous mantle flow, and (bottom row) second invariant of strain rate with a black contour outlining the cold plates.

linearly for longer slabs (supporting information Figure S18c). That might indicate increasing horizontal upper plate compression due to the larger mantle-wedge flow cell and enhanced shallow flow toward the slab induced by a longer initial slab (see supporting information Figure S19). As a result, the upper plate is under more compression (or less extension) and the island arc becomes more pronounced. The back-arc depression reaches a minimum depth at around a slab length of $l_s = 1000$ km (supporting information Figure S18d). This indicates that a shorter slab is not able to produce a large enough convection cell that would strongly pull down the upper plate (supporting information Figure S19d). On the other hand, the convection-cell size stagnates for long slabs as the slab tip becomes deep and the overall frictional forcing increases. Finally, a longer slab increases the width and the total area of the back-arc depression dramatically, again due to the larger induced flow cell (supporting information Figures S18e and S18f). The derived scaling laws for the individual topographic impacts of a variable-long slab are given in supporting information Figure S6.

3.5.2. Slab-Dip Angle

For all subduction parameters mentioned above, we systematically test here the influence of a variable shallow-depth slab dip, another crucial geometrical aspect of the subduction system. In these numerous additional experiments, we vary the initial, shallow-depth dip angle of the slab to cover a range between $15°-60°$ with a bending radius that evolves naturally up to the 2 Ma state (see Figure 9). In our simplified model setup, slabs dipping at lower angles than 15° tend to stick to the upper plate due to the larger interface between high-viscosity material, reduce the subducting-plate velocity, and thus inhibit actual subduction on a reasonable time scale (supporting information Figure S20). Additionally, shallow-depth slab dips
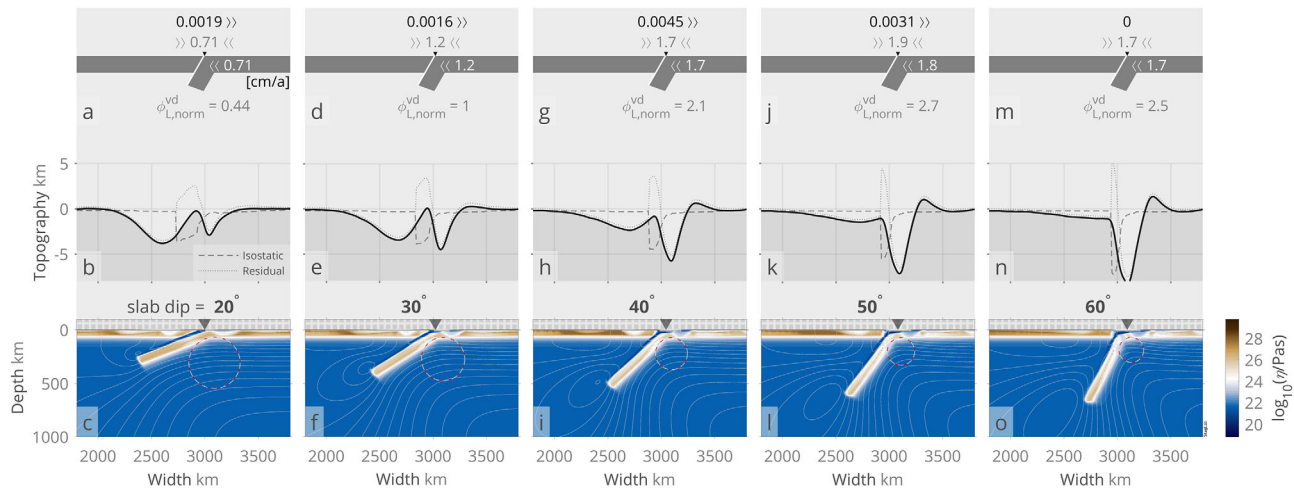
Figure 9. Comparison of different *control*-model experiments with variable initial shallow-depth slab dips ranging from (a, b, c) 20° to (m, n, o) 60°. Shown are, in the top row, tectonic parameters including current trench, convergence, and plate velocities, as well as relative bending dissipation ($\phi^{vd}_{L,norm}$). Further shown are close-ups of (middle row) topography including isostatic and residual components and (bottom row) effective viscosity with grey streamlines indicate flow direction. Red-white-dashed circles indicate minimum plate bending radius.

steeper than 60° would necessitate an unnatural strong curvature. In addition to our control model, we perform here seven additional suites of models to systematically test their individual impact of a variable shallow-depth slab dip (see Figure 10).

A quantitative measure of the lithospheric viscous bending dissipation normalized to the control model employing a 30° shallow-depth slab dip is given to characterize differently dipping slabs (see Figure 9). In these experiments, an increase in shallow-depth slab dip goes along with an increase in curvature. The
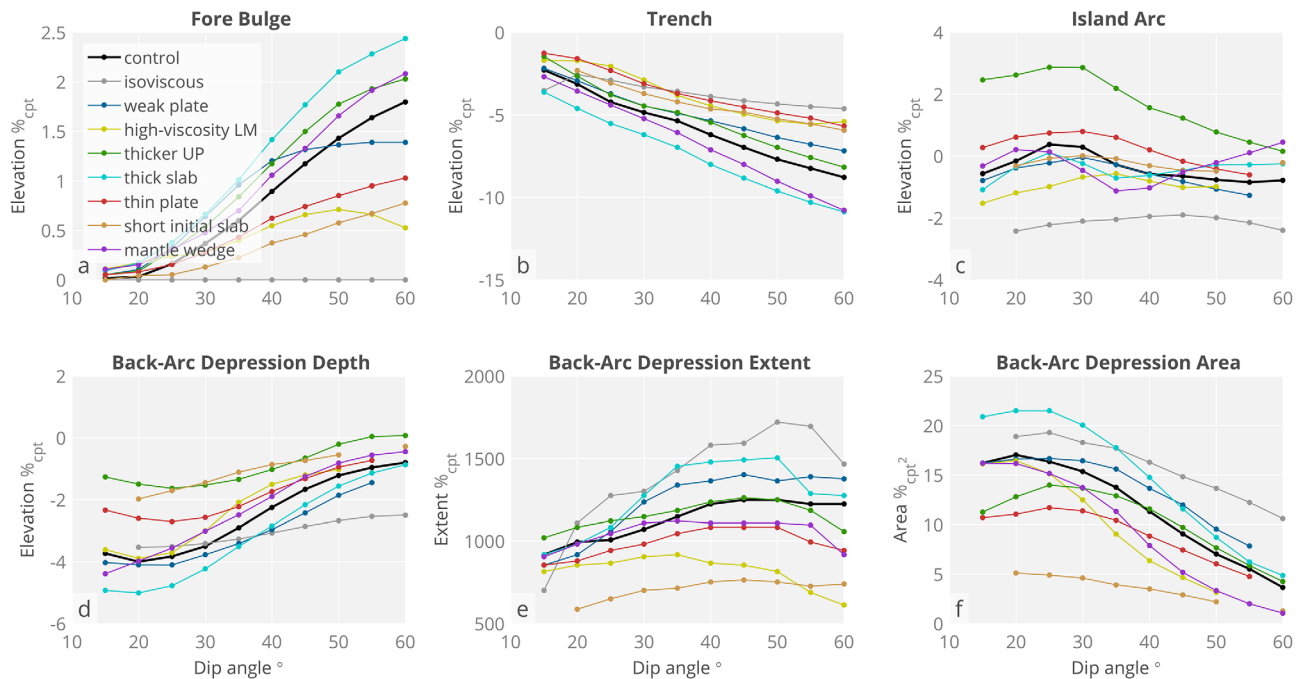
Figure 10. Graphs showing the effect of variable shallow-depth slab dip on (a) the height of the viscous fore-land bulge, (b) the depth of the subduction trench, (c) the height of the island-arc, and (d) the maximum depth, (e) the maximum horizontal extent, and (f) the maximum area of the back-arc depression. Shown are the *control* model (black) in comparison to an isoviscous model with no plate at all (*suite*5; grey), a model with a weaker plate (*suite*6; blue), a model with a high-viscosity lower mantle (*suite*8; yellow), a model with a thicker upper plate (*suite*7; green), a model with a thicker initial slab (*suite*2; cyan), a model with a younger and thinner subducting plate (*suite*4; red), a model with a shorter slab (*suite*3; orange), and a model with a low-viscosity mantle wedge (*suite*10; purple). Values on the y axis are given in percentage of (a–e) the initial, characteristic plate thickness, $d_{p0} = 93.2$ km, or (f) its square value, $d_{p0} = 8686$ km^2 (%$_{cpt}$ or %$_{cpt^2}$, respectively).

decreasing dissipation for steep slabs of $\geq 50°$ is therefore somewhat counterintuitive but can be explained by the slower lower-plate velocity, which counteracts the minor increase in curvature (see equation (18)).

In our experiments, the viscous fore-bulge becomes more pronounced for steeper-dipping slabs (Figure 10a). This results from a stronger bending of the subducting plate at the collision zone induced by the steeper subduction fault. The subduction trench becomes deeper for steeper dipping slabs in all the different suites presented here (Figure 10b). The trend is linear and an increase in dip angle of around $8-10°$ deepens the trench by 1 km. We observe a relatively (within ± 1 km) stable collisional height, which has a common maximum at $\sim 30°$ (Figure 10c). Shallow-dipping slabs ($<30°$) are not capable of producing strong plate compression due to the increased friction with the upper plate and their tendency to retreat, which generally causes extension in the upper plate. Steep-dipping slabs ($>30°$) localize on the other hand the downward suction force in the mantle wedge toward the subduction trench, which also reduces the overall height of the island-arc segment. The back-arc depression is deeper for shallow-dipping slabs (Figure 10d) and has a maximum width for slab-dip angles around $<45°$ (Figure 10e). Shallow-dipping slabs tend to increase the suction force on the upper plate, and thus also the back-arc depression, as the distance between the slab and the surface plate is shorter and stresses can be transmitted more efficiently. The basin becomes shorter for the same reason with steeper-dipping slabs for angles $>45°$, but also shortens slightly for shallower-dipping slabs at angles $<45°$, probably due to the increased sinking resistance of low-angled slabs (Figure 10e). The total deflected area of the back-arc depression has a maximum for slabs that dip at low angles of around $25°$ (Figure 10f). The total deflection then strongly decreases for steeper-dipping slabs.

3.5.3. 3-D Dynamics

Surface topography and subduction zones are both strongly affected by dynamics operating in all four dimensions (3-D space and time). Here, we reproduce therefore the control model in a 3-D geometry.

The first three-dimensional experiment reproduces the control 2-D experiment with a slab dip of $30°$ (Figures 11a and 11b). It has an initial subduction zone that spans throughout the whole model width. With
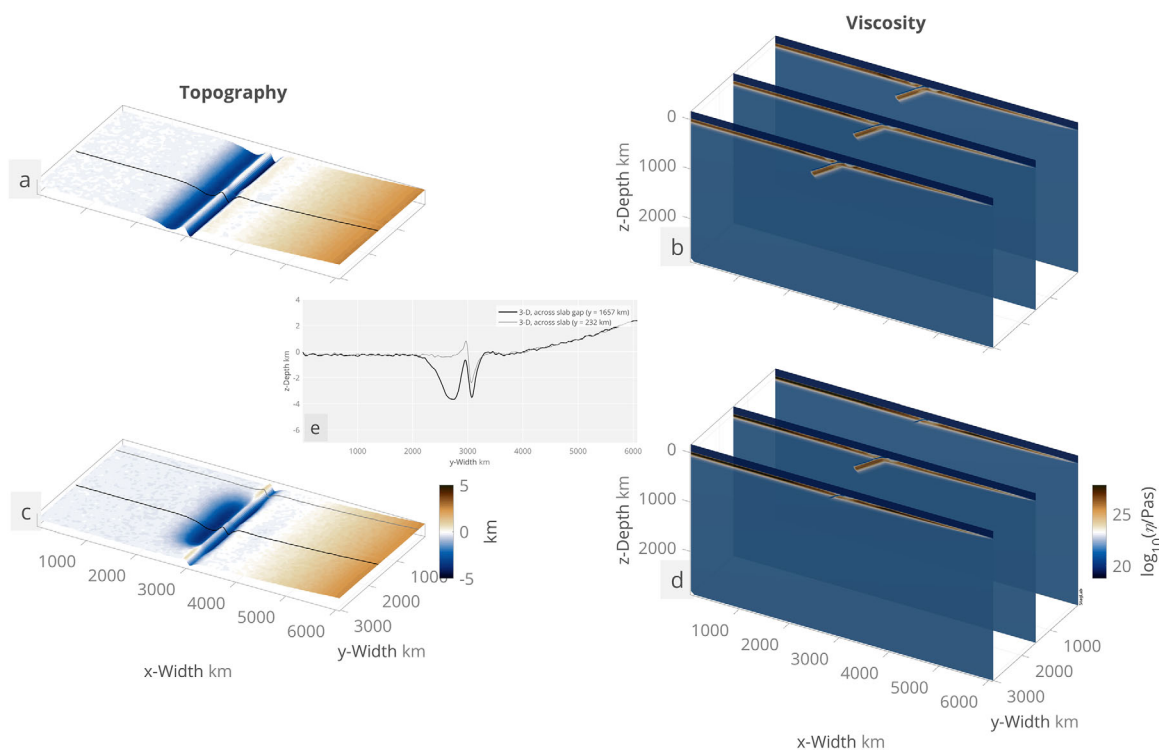
Figure 11. Comparison of surface topography between the two 3-D models with either (a, b) an initial, infinitely-wide slab (*run3d*; corresponding to the 2-D model) or (c, d) an initial finite-width slab (*run3d*$_{gap}$). Shown are (a, c) surface topography and (b, d) effective topography represented with three vertical slices along the model width showing. The black and grey lines in Figure 11c indicate the location of the corresponding topography profiles shown in Figure 11e across the slab (black) and across the slab gap (grey). The corresponding 2-D topography profiles for both models across the slab are additionally shown in Figure 1.

the wrap-around side boundaries, the subduction has therefore factually a 2-D geometry and is directly comparable to the results above. Not surprisingly, the flow (dominated by the sinking plate) is entirely poloidal according to the 2-D experiments, and the topographic signal matches the one from the 2-D model. In a second 3-D experiment, we limit the lateral extent of the initial slab (Figures 11c and 11d): The slab spans 60% of the model width. The topography above the sinking slab is still in good agreement with the 2-D model even though smaller trench and island-arc amplitudes are observed (Figure 1b). This is caused by the reduced net driving force: The much smaller slab pull (due to the missing slab portion) is now counteracted by the only slightly smaller resisting forces (due to the smaller total slab area but the unaltered surface area of the subducting plate that has to be dragged toward the trench).

Another, interesting comparison can also be made between the topography across the subduction zone where the slab is missing and the topography across where the slab is present (see Figure 11e): The topography along the side of the slab has a shallower trench, a higher island-arc and lacks the downward deflection of the entire upper plate portion close to the trench. The trench is shallower due to the missing slab pull, which also causes a higher island-arc. The higher island-arc is additionally supported by an increased compression in the upper plate due to the absence of a slab in these regions that would otherwise guide the plate downward into the mantle. The lack of the back-arc depression can finally be explained by the missing slab suction that is otherwise transmitted through the mantle wedge.

4. Discussion

A model, like the one presented here, linking Earth's dynamic interior with its surface, is crucial to better understand the regional topography at a convergent plate boundary. The unique, extensive parameter testing performed here using this model additionally allows us to better understand the individual potential of the various important subduction parameters to deflect the top boundary of our planet. Moreover, the temporal evolution of individual subduction zones, and more specifically their buoyancy, rheology, and geometry, might be constrained as accurate topography back through time is often available in the geologic record.

4.1. General-Topography Controls

Similarly to *Zhong and Gurnis* [1992], we find here that the weak subduction fault is responsible for preventing a more symmetrical surface depression by directing some of the forcing toward the trench. The subduction fault is additionally found to act as a geometrical guide to lower-plate subduction over short-time scales (i.e., a few Ma). This geometric effect is more pronounced in the presence of a thick upper plate when this geometric guide remains effective to deeper levels.

Additionally, we find that a stiff upper boundary layer significantly filters the overall topographic signal caused by dynamic forcing originating in the mantle: Topographic amplitudes get damped and short-wavelength mantle stresses are converted into long-wavelength surface deflections. This is due to the fact that bending a higher-viscosity plate needs more work, which is reflected in the increasing amount of viscous bending dissipation toward stronger plates (see supporting information Figure S10a, S10d, S10g, S10j, and 10m).

Similar general effects on subduction-zone topography are observed for rheological changes in the slab's surrounding medium. An increase of mantle viscosity with depth or pressure mimics a decrease in slab pull due to more sinking resistance on the slab and thereby decreases the overall topographic amplitudes, as was similarly suggested in *Hager* [1984].

4.2. Regional-Topography Controls

Our model allows to additionally capture the regional topographic variations at a subduction zone due to the consideration of lateral viscosity variations like the high-viscosity slab, the weak subduction channel, or the low-viscosity mantle wedge [see *Cadek and Fleitout*, 2003; *Kaban et al.*, 2014; *Gérault et al.*, 2015]. Apart from the general controls on surface topography at a convergent boundary, we can therefore discriminate the more specific links between subduction parameters and regional topographic characteristics and provide corresponding scaling laws where applicable.

4.2.1. Comparison to Observations

Statistical compilations of observations on present-day Earth indicate only a few clear relationships between subduction parameters and regional surface topography at subduction zones [e.g., *Jarrard*, 1986; *Lallemand et al.*, 2005].

The viscous fore-bulge is found to have a height of around 100–500 m [e.g., *McAdoo et al.*, 1985]. Our models indicate that the fore-bulge generally increases for steeper-dipping slabs and that much higher bulges than the observed range are only prevented if either slab pull is reduced by, for example, a high-viscosity lower mantle, or plate bending is facilitated by, for example, a thin subducting plate (see Figure 10a).

Hilde and Uyeda [1983] realized that subduction trenches on Earth are deeper with older, and hence heavier and thicker subducting plates. Additionally, deep trenches correlate well with steeply-dipping slabs [*Hilde and Uyeda*, 1983; *Jarrard*, 1986] and fast convergence rates [*Grellet and Dubois*, 1982]. Our modeling is in full agreement with all of these observations and additionally indicates shallower trenches for lower slab-mantle viscosity contrast (see Figures 6b and 10b).

There is little systematic observational evidence on the island-arc elevation relative to subduction parameters. Our models show that apart from extreme subduction-parameter values there is generally little dependence of the island-arc height on most subduction parameters (Figure 6c). Only thick upper plates appear to induce significantly higher arcs (see Figure 10c).

Again, there is little systematic observational evidence on the elevation of the back-arc depression: The back-arc depression on Earth is often overprinted by the results of volcanism, collisional tectonics, or sediment deposition [see e.g., *Amante and Eakins*, 2009; *Ryan et al.*, 2009, and Figure 3]. Our models indicate a strong correlation of deep basins with large negative slab buoyancy by, for example, a thicker subducting plate (Figures 6d–6f and 10d–10f). Additionally, we show here that shallow-dipping slabs deepen the back-arc basins significantly (Figures 10d–10f). A more detailed description of our findings in relation to previous studies is, for each topographic feature, given below.

4.2.2. Viscous Fore-Bulge

The viscous fore-bulge observed in our models is mainly caused by the active downward bending of the high-viscosity plate at the plate interface, which causes viscous deformation in the plate [*Melosh*, 1978; *Gurnis et al.*, 1996]. It is therefore not surprising that its height is strongly controlled by the shallow-depth slab dip angle (and plate curvature) and the slab pull force (i.e., active bending): The fore bulge is more pronounced for steeper-dipping and heavier slabs (see Figure 10a). As an increase in mantle viscosity with depth also reduces the pull of the slab, the fore-bulge height is also dependent on the radial mantle viscosity structure. This can be observed in cases where a steep and thus deep-reaching slab starts to experience more resistance from the high-viscosity lower mantle.

4.2.3. Subduction Trench

Subduction trenches are mainly the result of the downward force (i.e., slab pull) acting on the subducting plate at the plate interface. This slab pull and hence also the trench depth are strongly dependent on both slab buoyancy and slab-sinking resistance (see Figure 6b). The linear topographic response of the subduction trench to a change in slab buoyancy found here (see supporting information Figure S6b) is also in accordance with previous findings indicating that trench depth is in a linear relationship with slab-mantle temperature contrast [*Zhong and Gurnis*, 1992] or, in other words, with slab buoyancy. *Hilde and Uyeda* [1983] showed that trench depth further increases with the age of the subducting plate portion, which is in accordance to our model with a thinner (i.e., younger) plate that produces a shallower trench (Figure 10b and supporting information Figure S14). This might, for the most part, be caused by the increased negative buoyancy of older slabs, as older and thus heavier slabs cause deeper trenches (supporting information Figure S6b). Subduction parameters that reduce the net driving force of a slab like a high-viscosity lower mantle or a shallow-depth slab dip are consequently found to reduce trench depth significantly (see Figures 9 and 10b). The latter is in accordance to previous modeling results [*Zhong and Gurnis*, 1992, 1994; *Gurnis et al.*, 1996] and to present-day observations, where shallow trenches correlate generally with shallow-dipping slabs [*Hilde and Uyeda*, 1983; *Jarrard*, 1986] or slow convergence rates [*Grellet and Dubois*, 1982]. The dependency of trench depth to shallow-depth slab dip angle is here found to be linear in accordance to *Zhong and Gurnis* [1994] for all cases without an UM-LM viscosity jump (Figure 10b): An increase of 20° in dip angle deepens the trench by 5% of plate thickness. The linear relationship breaks down, if the model

includes a higher-viscosity lower mantle: The increasing resistance of the high-viscosity lower mantle during slab sinking reduces the net driving force of the heavy slab.

Moreover, we find that the trench is generally shallower in the isoviscous or weak-plate experiments compared to the control experiments (Figure 10b and supporting information Figure S11b). This indicates that stress is transmitted more efficiently along high viscous slabs, a process first introduced in *Elsasser* [1971]. In order to obtain a narrow and deep trench that is in agreement to observations (see e.g., Figures 3b and 3c), *Zhong and Gurnis* [1992] showed that a sufficiently high-viscosity contrast of $\Delta\eta_{LA} > 100$ between lithosphere and upper mantle is necessary. For viscosity contrasts $\Delta\eta_{LA} < 100$, we indeed observe a broader and shallower trench than for larger viscosity contrasts $\Delta\eta_{LA} > 100$. Additionally, we find here that the trench elevation becomes independent of the plate-mantle viscosity contrast above $\Delta\eta_{LA} = 200$ (see Figure 6b).

4.2.4. Island-Arc

The island-arc is a feature within the compressive regime of the plate collision zone (see supporting information Figure S21). While the island-arc height is barely affected by changes in the buoyancy of the system, it strongly depends on the rheology (see Figure 6c): The island-arc is hardly observable for low plate-mantle viscosity contrasts and rises strongly toward higher contrast until its height becomes nearly constant for $\Delta\eta_{LA} > 200$. More specifically, we find that the island-arc is, for the most part, controlled by upper plate strength, with weak plates causing low elevation and strong plates causing high elevation (see Figure 10c). A comparable correlation with plate strength is also found for high collisional topography on continental upper plates [*Pusok and Kaus*, 2015]. By controlling the flow-cell size in the mantle wedge, the length of the slab strongly affects additionally the amount of compression in the collision zone and hence the topographic elevation of the island-arc (supporting information Figures S18c and S19).

4.2.5. Back-Arc Depression

The back-arc depression depth is nearly independent of rheology. It is, however, found to be strongly controlled by the slab buoyancy (see Figure 6d) that controls the total amount of forcing available, and the geometry of the system (see Figure 10d) that controls where these stresses are most-efficiently transmitted to the surface. As mentioned above and introduced by *Elsasser* [1971], a shallower-dipping slab transfers stresses to the surface rather through the mantle wedge (slab suction) than along the slab itself (slab pull). Topographic depressions tend therefore to be amplified around the trench when the slab dips at a high angle and further away on the upper plate in the back arc when the slab dips at a low angle [see also *Gurnis et al.*, 1996]. Decreasing slab suction via a higher, radial mantle-viscosity gradient causes therefore also a shallower back-arc depression (see supporting information Figure S16), which is in accordance to the previous findings of *Billen et al.* [2003]. The horizontal extent and the resulting total area of the back-arc depression behave similarly: The buoyancy and geometry of the system have the key control, while the rheology appears to be less important (see Figures 6e and 6f). It might therefore be possible to infer past slab geometry and buoyancy using the collected record of sedimentary patterns related to continental inundation.

The back-arc depression is one consistently prominent feature occurring throughout all the models presented here. There is observational constraint on the existence of the broad downward deflection in the back-arc region: The, for its plate age, anomalously-deep basin in the back of the Marianas arc is one example [e.g., *Watanabe et al.*, 1977]. In nature, the back-arc basin is, however, rarely clearly visible (see e.g., Figure 3); It is, for example, often overprinted by collisional topographic highs (e.g., an island-arc) or a continental margin with its thick, light crustal layer [see e.g., *Amante and Eakins*, 2009; *Ryan et al.*, 2009]. The latter then additionally causes an average altitude of the upper plate that is often significantly higher than that of the lower plate (see e.g., Figure 3c). In order to eliminate or at least reduce the anomalously deep basins on the upper plate in numerical models like the one presented here, *Billen and Gurnis* [2003] proposed the addition of a low-viscosity mantle wedge. Indeed, our experiments with a low-viscosity mantle wedge reproduce the finding that it reduces topography amplitudes on the upper plate (see Figure 10d). Our modeling study indicates therefore that both steep slabs and minor coupling in the mantle wedge might help to reduce the discrepancy between modeled and observed back-arc depressions. Another way to reduce deep back-arc depressions could be "slab anchoring" [*Gérault et al.*, 2015], where the long, nearly vertical slab is dynamically supported by the high-viscosity lower mantle it is dipping in. Compositional buoyancy of a slab segment, which could result in a positively buoyant slab, would be yet another possibility to reduce a deep back-arc depression. Such buoyant slab segments then might foster an opposed topographic uplift on the upper plate [*Dávila and Lithgow-Bertelloni*, 2015].
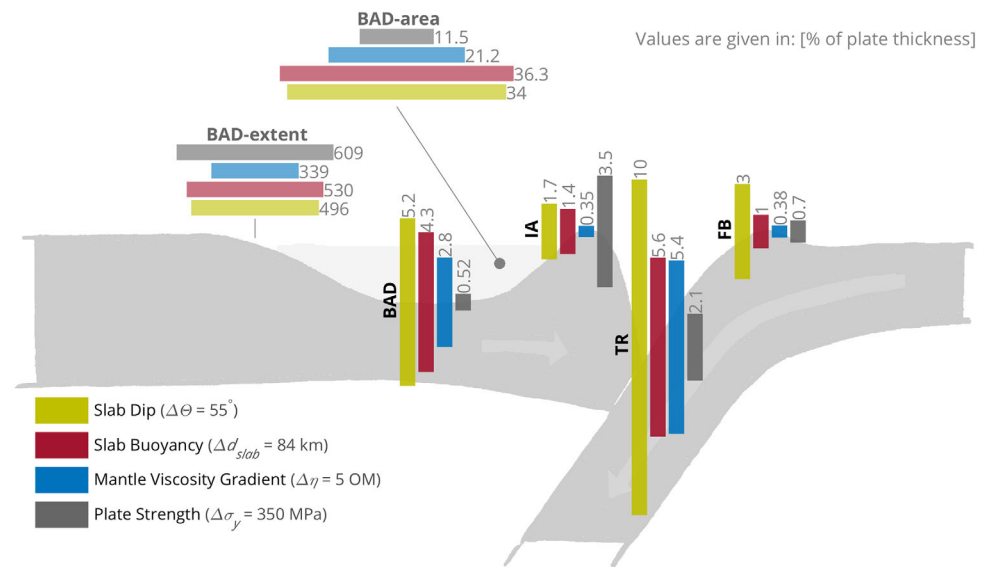
Figure 12. Overview over the potential range over which individual subduction parameters can spatially alter the individual topographic features of a collisional plate boundary on an Earth-like planet. The height of a bar indicates the maximal spatial variation occurring in the experiments presented here over an Earth-like parameter range given in the figure legend. Values are given in percentage of plate thickness. The individual topographic features indicated are fore-bulge height (FB), trench depression (TR), island-arc height (IA), and back-arc depression (BAD), extent (BAD-extent), and area (BAD-area).

4.3. Relative Topography Contributions on Earth

Figure 12 gives an overview of the individual importance of the different driving, resisting and geometrical aspects of a subduction system for each of the topographic indication points. Each of the colored bars indicates the maximum topographic variation found in our control model using an Earth-like parameter range. Shown are the results of suites of experiments varying the slab thickness (representing buoyancy aspects), the plate strength and the mantle viscosity (both representing rheological aspects), and the shallow-depth slab dip angle (representing geometric aspects). The given parameter ranges (considered Earth-like and within reach of our numerical model) are for shallow-depth slab dip $\Delta\theta$=55° (15°−60°), for slab buoyancy/thickness Δd_s=84 km (50−134 km), for radial mantle-viscosity gradient ΔV_{act}=3 × 10⁻⁶ m³/mol (0−3 × 10⁻⁶ m³/mol) corresponding to five orders of magnitude viscosity increase (0−5 OM) through the mantle, and for plate strength $\Delta\sigma_y$=350 MPa (50−400 MPa).

From this compilation, it is obvious that the shallow-depth slab dip angle has a key control on all the topographic features considered here; it is the main agent controlling fore-bulge height, trench depth, and width of the back-arc depression when varying subduction parameters across an Earth-like range. The slab buoyancy is the second most important control mechanism strongly shaping for example the trench topography. Its importance on surface topography has been previously stressed when slab pull and slab suction were found to be the dominating forces in Earth's mantle [*Hilde and Uyeda*, 1983]. Similarly, the back-arc depression depth and area are mainly controlled by both slab dip and slab buoyancy. In contrast, the island-arc is, as the only considered topographic feature, mainly controlled by the strength of the plate. The plate strength further (together with the slab dip and buoyancy) strongly impacts the back-arc depression width. Finally, the radial mantle viscosity changes have an overall smaller, but nonnegligible effect on surface topography.

This compilation indicates further that the subduction trench is the most variable topographic feature in terms of vertical amplitude of all the regional topographic characteristics considered here. The overall importance of slab buoyancy and shallow-depth slab dip to control surface deflection at convergent margins indicates that the amount of forcing and the actual location in the mantle, where it is applied to, are the two crucial factors for a subduction system's surface topography.

4.4. Model Limitations

Most experiments presented here are carried out in a 2-D Cartesian geometry. This neglects the curvature of the Earth and assumes that the subduction zones are effectively infinitely long, whereas in nature,

subduction zones are usually around 2000−4000 km long. This approximation limits therefore the significance of our results to wide subduction zones and/or central subduction-zone segments: Narrow subduction zones or parts of subduction zones near their lateral edges are likely to be strongly influenced by the existence of 3-D toroidal mantle flow around slab edges [*Funiciello et al.*, 2004], which causes slabs and the subduction trenches above to become arcuate [*Crameri and Tackley*, 2014]. But even the central parts of wide slabs can be strongly affected by 3-D mantle flow features like "back-slab spiral flow" (i.e., the combination of poloidal flow and lateral, trench-parallel flow) and regional flow stagnation zones that can lead to "slab tunnelling" followed by the formation of multiarcuate slabs and trenches [*Crameri and Tackley*, 2014].

In addition, we only model ocean-ocean collision zones, whereas on Earth most subduction zones are under the influence of an adjacent continent. Including the dynamic effects of continental lithosphere might therefore be the next logic step following the approach of this study.

The models used here use a viscoplastic rheology, neglecting possible effects of elasticity like lithospheric flexure. Previous studies have shown that the difference between viscoplastic and viscoelastoplastic models is minor in terms of Earth-like subduction dynamics [e.g., *Schmeling et al.*, 2008]. Elasticity might be important in the lithosphere on short-wavelength (i.e., on the lithospheric flexural length), but probably has little effect on dynamic topography, which acts on larger wavelengths spanning around 100 km [*Zhong and Gurnis*, 1992, 1994]. However, possible effects of elastic stresses on long-wavelength surface topography should be carefully examined in the future.

There is a slight discrepancy between our model and nature, with Earth's mantle having around an order of magnitude higher Rayleigh number. Our tests show that a higher Rayleigh number increases overall plate speed and thus slightly amplifies both trench and back-arc depression (see supporting information Figure S22). There are other compositional and rheologic effects that cannot be fully considered by our models that might affect a plate's natural bending radius. Our additional tests show that a higher initial bending radius generally slightly reduces the island-arc height and back-arc depression (see supporting information Figure S23). An important aspect in the coupling between slab dynamics and surface topography is the ability to transmit stress from the deep slab to the surface through the mantle wedge. Factors currently inducing big uncertainty there are for example the mantle rheology and compositional heterogeneities. A power law rheology like dislocation creep or the presence of low-viscosity zones due to melting or volatiles (e.g., H_2O or CO_2) certainly play an important role in weakening the link between mantle flow and surface topography and should be considered in future studies.

5. Conclusions

We tested the crucial interaction between the key subduction parameters and regional surface-plate deflection in systematic suites of experiments using a suitably-simple, two-dimensional model of mantle convection that is capable of producing self-consistent single-sided subduction. A widely-used fixed, flat plate surface was shown to be an oversimplification to our model: Calculated, traction-derived subduction zone topography in models using a free-slip surface was found to be strongly influenced by unnatural plate bending and stresses at the trench. Our free-slip model could therefore not reproduce the steep and high amplitude topography of a converging plate boundary.

The numerous experiments in this study were subsequently computed with a model using a free-surface boundary condition. We diagnosed these experiments with various physical complexities such as the different topographic components or the viscous dissipation in the lithosphere due to bending. These results provide insight into the specific importance of the multiple and diverse subduction parameters regarding each of four dominant surface topography characteristics at a convergent boundary.

We found that the geometric aspect (i.e., the shallow-depth slab dip) and the buoyancy aspect of a subduction system (i.e., slab buoyancy) dominate most surface topography signals. The back-arc depression caused by a shallow-dipping slab is, for example, shown to merge with the trench depression for steeper dipping slabs. In fact we show that abnormally deep back-arc depressions generally observed in numerical models are prevented with a combination of a low-viscosity mantle wedge and steeply dipping shallow slabs. The island-arc elevation and the lateral extent of the back-arc depression are exceptions to this trend: The island-arc is mainly controlled by horizontal, tectonic stresses and thus mainly by the rheological aspect of

the subduction system (i.e., the strength of the plate). The lateral back-arc depression extent is similarly strongly controlled by the strength of the upper plate. Overall, a strong plate is harder to bend (e.g., produces more viscous bending dissipation) and hence dampens the topographic amplitudes by converting short-wavelength mantle stresses into long-wavelength surface deflections. The radial mantle viscosity, another rheological aspect, adds a nonnegligible, but overall only intermediate contribution to the topographic amplitude over the short period in the parameter range tested here. A longer slab, the second-most important geometric aspect, induces a larger flow cell in the mantle wedge with enhanced shallow flow toward the slab. This then causes more compression in the plate above through viscous coupling, which pronounces the island-arc. Finally, the pooling of our experiments indicates that the depth of the subduction trench is the dynamically most variable regional topographic feature on Earth.

These findings reveal the complex interplay between mantle dynamics and surface topography at convergent plate boundaries in a more complete framework. This study sets therefore an important basis for a subduction-parameter constraint via surface-topography observations for present-day Earth but, crucially, also through time.

References

Amante, C., and B. Eakins (2009), ETOPO1 1 arc-minute global relief model: Procedures, data sources and analysis, NOAA Tech. Mem. NES-DIS NGDC-24, Natl. Geophys. Data Cent., NOAA, doi:10.7289/V5C8276M.

Arrial, P.-A., and M. I. Billen (2013), Influence of geometry and eclogitization on oceanic plateau subduction, *Earth Planet. Sci. Lett.*, *363*, 34–43.

Barazangi, M., and B. L. Isacks (1976), Spatial distribution of earthquakes and subduction of the Nazca plate beneath South America, *Geology*, *4*(11), 686–692.

Billen, M. I., and M. Gurnis (2001), A low viscosity wedge in subduction zones, *Earth Planet. Sci. Lett.*, *193*(1-2), 227–236.

Billen, M. I., and M. Gurnis (2003), Comparison of dynamic flow models for the Central Aleutian and Tonga-Kermadec subduction zones, *Geochem. Geophys. Geosyst.*, *4*(4), 1035, doi:10.1029/2001GC000295.

Billen, M. I., M. Gurnis, and M. Simons (2003), Multiscale dynamics of the Tonga-Kermadec subduction zone, *Geophys. J. Int.*, *153*(2), 359–388.

Borland, D., and R. M. T. Ii (2007), Rainbow color map (still) considered harmful, *IEEE Comput. Graph. Appl.*, *27*(2), 14–17.

Boschi, L., C. Faccenna, and T. W. Becker (2010), Mantle structure and dynamic topography in the Mediterranean Basin, *Geophys. Res. Lett.*, *37*, L20303, doi:10.1029/2010GL045001.

Braun, J. (2010), The many surface expressions of mantle dynamics, *Nat. Geosci.*, *3*(12), 825–833.

Buffett, B. A. (2006), Plate force due to bending at subduction zones, *J. Geophys. Res.*, *111*, B09405, doi:10.1029/2006JB004295.

Cadek, O., and L. Fleitout (2003), Effect of lateral viscosity variations in the top 300 km on the geoid and dynamic topography, *Geophys. J. Int.*, *152*(3), 566–580, doi:10.1046/j.1365-246x.2003.01859.x.

Cazenave, A., A. Souriau, and K. Dominh (1989), Global coupling of Earth surface topography with hotspots, geoid and mantle heterogeneities, *Nature*, *340*(6228), 54–57.

Conrad, C. P., and B. H. Hager (1999), Effects of plate bending and fault strength at subduction zones on plate dynamics, *J. Geophys. Res.*, *104*(B8), 17,551–17,571, doi:10.1029/1999JB900149.

Conrad, C. P., and C. Lithgow-Bertelloni (2002), How mantle slabs drive plate tectonics, *Science*, *298*(5591), 207–209, doi:10.1126/science.1074161.

Crameri, F., and P. J. Tackley (2014), Spontaneous development of arcuate single-sided subduction in global 3-D mantle convection models with a free surface, *J. Geophys. Res. Solid Earth*, *119*, 5921–5942, doi:10.1002/2014JB010939.

Crameri, F., and P. J. Tackley (2015), Parameters controlling dynamically self-consistent plate tectonics and single-sided subduction in global models of mantle convection, *J. Geophys. Res. Solid Earth*, *120*, 3680–3706, doi:10.1002/2014JB011664.

Crameri, F., and P. J. Tackley (2016), Subduction initiation from a stagnant lid and global overturn: New insights from numerical models with a free surface, *Prog. Earth Planet. Sci.*, *3*, 1–19, doi:10.1186/s40645-016-0103-8.

Crameri, F., H. Schmeling, G. J. Golabek, T. Duretz, R. Orendt, S. J. H. Buiter, D. A. May, B. J. P. Kaus, T. V. Gerya, and P. J. Tackley (2012a), A comparison of numerical surface topography calculations in geodynamic modelling: An evaluation of the 'sticky air' method, *Geophys. J. Int.*, *189*(1), 38–54, doi:10.1111/j.1365-246X.2012.05388.x.

Crameri, F., P. J. Tackley, I. Meilick, T. V. Gerya, and B. J. P. Kaus (2012b), A free plate surface and weak oceanic crust produce single-sided subduction on Earth, *Geophys. Res. Lett.*, *39*, L03306, doi:10.1029/2011GL050046.

Cruciani, C., E. Carminati, and C. Doglioni (2005), Slab dip vs. lithosphere age: No direct function, *Earth Planet. Sci. Lett.*, *238*(3–4), 298–310.

Davies, G. F. (1981), Regional compensation of subducted lithosphere: Effects on geoid, gravity and topography from a preliminary model, *Earth Planet. Sci. Lett.*, *54*(3), 431–441.

Davies, G. F., and F. Pribac (1993), Mesozoic seafloor subsidence and the Darwin Rise, past and present, in *The Mesozoic Pacific: Geology, Tectonics, and Volcanism*, pp. 39–52, AGU, Washington, D. C.

Dávila, F. M., and C. Lithgow-Bertelloni (2015), Dynamic uplift during slab flattening, *Earth Planet. Sci. Lett.*, *425*, 34–43, doi:10.1016/j.epsl.2015.05.026.

Dávila, F. M., C. Lithgow-Bertelloni, and M. Giménez (2010), Tectonic and dynamic controls on the topography and subsidence of the Argentine Pampas: The role of the flat slab, *Earth Planet. Sci. Lett.*, *295*(1-2), 187–194.

de Bremaecker, J.-C. (1977), Is the oceanic lithosphere elastic or viscous?, *J. Geophys. Res.*, *82*(14), 2001–2004.

Eakin, C. M., C. Lithgow-Bertelloni, and F. M. Dávila (2014), Influence of Peruvian flat-subduction dynamics on the evolution of western Amazonia, *Earth Planet. Sci. Lett.*, *404*, 250–260.

Elsasser, W. M. (1971), Sea-floor spreading as thermal convection, *J. Geophys. Res.*, *76*(5), 1101–1112.

Flament, N. (2014), Linking plate tectonics and mantle flow to Earth's topography, *Geology*, *42*(10), 927–928.

Flament, N., M. Gurnis, and R. D. Müller (2013), A review of observations and models of dynamic topography, *Lithosphere*, *5*(2), 189–210.

Forsyth, D., and S. Uyeda (1975), On the relative importance of the driving forces of plate motion*, *Geophys. J. R. Astron. Soc.*, *43*(1), 163–200.

Forte, A. M., W. R. Peltier, A. M. Dziewonski, and R. L. Woodward (1993), Dynamic surface topography: A new interpretation based upon mantle flow models derived from seismic tomography, *Geophys. Res. Lett.*, *20*(3), 225–228.

Forte, A. M., S. Quéré, R. Moucha, N. A. Simmons, S. P. Grand, J. X. Mitrovica, and D. B. Rowley (2010), Joint seismic-geodynamic-mineral physical modelling of African geodynamics: A reconciliation of deep-mantle convection with surface geophysical constraints, *Earth Planet. Sci. Lett.*, *295*(3–4), 329–341.

François, T., E. Burov, P. Agard, and B. Meyer (2014), Buildup of a dynamically supported orogenic plateau: Numerical modeling of the Zagros/Central Iran case study, *Geochem. Geophys. Geosyst.*, *15*, 2632–2654, doi:10.1002/2013GC005223.

Funiciello, F., C. Faccenna, D. Giardini, and K. Regenauer-Lieb (2003), Dynamics of retreating slabs: 2. Insights from three-dimensional laboratory experiments, *J. Geophys. Res.*, *108*(B4), 2207, doi:10.1029/2001JB000896.

Funiciello, F., C. Faccenna, and D. Giardini (2004), Role of lateral mantle flow in the evolution of subduction systems: Insights from laboratory experiments, *Geophys. J. Int.*, *157*(3), 1393–1406.

Garel, F., S. Goes, D. R. Davies, J. H. Davies, S. C. Kramer, and C. R. Wilson (2014), Interaction of subducted slabs with the mantle transition-zone: A regime diagram from 2-D thermo-mechanical models with a mobile trench and an overriding plate, *Geochem. Geophys. Geosyst.*, *15*, 1739–1765, doi:10.1002/2014GC005257.

Gérault, M., L. Husson, M. S. Miller, and E. D. Humphreys (2015), Flat-slab subduction, topography, and mantle dynamics in southwestern Mexico, *Tectonics*, *34*, 1892–1909, doi:10.1002/2015TC003908.

Grellet, C., and J. Dubois (1982), The depth of trenches as a function of the subduction rate and age of the lithosphere, *Tectonophysics*, *82*(1), 45–56.

Gurnis, M. (1993), Phanerozoic marine inundation of continents driven by dynamic topography above subducting slabs, *Nature*, *364*(6438), 589–593.

Gurnis, M., C. Eloy, and S. Zhong (1996), Free-surface formulation of mantle convection–II. Implication for subduction-zone observables, *Geophys. J. Int.*, *127*(3), 719–727.

Hager, B. H. (1984), Subducted slabs and the geoid: Constraints on mantle rheology and flow, *J. Geophys. Res.*, *89*(B7), 6003–6015.

Hager, B. H., R. W. Clayton, M. A. Richards, R. P. Comer, and A. M. Dziewonski (1985), Lower mantle heterogeneity, dynamic topography and the geoid, *Nature*, *313*(6003), 541–546.

Hilde, T. W., and S. Uyeda (1983), Trench depth: Variation and significance, in *Geodynamics of the Western Pacific-Indonesian Region*, pp. 75–89, AGU, Washington, D. C.

Hirth, G., and D. L. Kohlstedt (1996), Water in the oceanic upper mantle: Implications for rheology, melt extraction and the evolution of the lithosphere, *Earth Planet. Sci. Lett.*, *144*(12), 93–108.

Hoggard, M. J., N. White, and D. Al-Attar (2016), Global dynamic topography observations reveal limited influence of large-scale mantle flow, *Nat. Geosci.*, *9*(6), 456–463.

Hu, J., and L. Liu (2016), Abnormal seismological and magmatic processes controlled by the tearing South American flat slabs, *Earth Planet. Sci. Lett.*, *450*, 40–51.

Hu, J., L. Liu, A. Hermosillo, and Q. Zhou (2016), Simulation of late Cenozoic South American flat-slab subduction using geodynamic models with data assimilation, *Earth Planet. Sci. Lett.*, *438*, 1–13.

Husson, L., M. Bernet, S. Guillot, P. Huyghe, J.-L. Mugnier, A. Replumaz, X. Robert, and P. Van der Beek (2014), Dynamic ups and downs of the Himalaya, *Geology*, *42*(10), 839–842.

Isacks, B. L., and M. Barazangi (1977), Geometry of Benioff zones, in *Island Arcs, Deep Sea Trenches and Back-Arc Basins*, pp. 99–114, AGU, Washington, D. C.

Jadamec, M. A., M. I. Billen, and S. M. Roeske (2013), Three-dimensional numerical models of flat slab subduction and the denali fault driving deformation in south-central alaska, *Earth Planet. Sci. Lett.*, *376*, 29–42.

Jarrard, R. D. (1986), Relations among subduction parameters, *Rev. Geophys.*, *24*(2), 217–284.

Jones, C. H., G. L. Farmer, B. Sageman, and S. Zhong (2011), Hydrodynamic mechanism for the Laramide orogeny, *Geosphere*, *7*(1), 183–201.

Kaban, M. K., P. Schwintzer, and C. Reigber (2004), A new isostatic model of the lithosphere and gravity field, *J. Geodes.*, *78*(6), 368–385.

Kaban, M. K., A. G. Petrunin, H. Schmeling, and M. Shahraki (2014), Effect of decoupling of lithospheric plates on the observed geoid, *Surv. Geophys.*, *35*(6), 1361–1373, doi:10.1007/s10712-014-9281-3.

Karig, D. E. (1971), Origin and development of marginal basins in the western Pacific, *J. Geophys. Res.*, *76*(11), 2542–2561.

King, S. D. (2009), On topography and geoid from 2-D stagnant lid convection calculations, *Geochem. Geophys. Geosyst.*, *10*, Q03002, doi:10.1029/2008GC002250.

Lallemand, S., A. Heuret, and D. Boutelier (2005), On the relationships between slab dip, back-arc stress, upper plate absolute motion, and crustal nature in subduction zones, *Geochem. Geophys. Geosyst.*, *6*, Q09006, doi:10.1029/2005GC000917.

Le Stunff, Y., and Y. Ricard (1995), Topography and geoid due to lithospheric mass anomalies, *Geophys. J. Int.*, *122*(3), 982–990.

Lithgow-Bertelloni, C., and P. G. Silver (1998), Dynamic topography, plate driving forces and the African superswell, *Nature*, *395*(6699), 269–272.

Liu, L., and M. Gurnis (2010), Dynamic subsidence and uplift of the Colorado Plateau, *Geology*, *38*(7), 663–666.

Liu, L., S. Spasojević, and M. Gurnis (2008), Reconstructing Farallon plate subduction beneath North America back to the Late Cretaceous, *Science*, *322*(5903).

Manea, V. C., M. Pérez-Gussinyé, and M. Manea (2012), Chilean flat slab subduction controlled by overriding plate thickness and trench rollback, *Geology*, *40*(1), 35–38.

Matsumoto, T., and Y. Tomoda (1983), Numerical simulation of the initiation of subduction at the fracture zone, *J. Phys. Earth*, *31*(3), 183–194.

McAdoo, D. C., C. F. Martin, and S. Poulouse (1985), Seasat observations of flexure: Evidence for a strong lithosphere, *Tectonophysics*, *116*(3), 209–222.

Melosh, H. J. (1978), Dynamic support of the outer rise, *Geophys. Res. Lett.*, *5*(5), 321–324.

Mitrovica, J. X., C. Beaumont, and G. T. Jarvis (1989), Tilting of continental interiors by the dynamical effects of subduction, *Tectonics*, *8*(5), 1079–1094.

Moucha, R., and A. M. Forte (2011), Changes in African topography driven by mantle convection, *Nat. Geosci.*, *4*(10), 707–712.

Moucha, R., A. M. Forte, D. B. Rowley, J. X. Mitrovica, N. A. Simmons, and S. P. Grand (2009), Deep mantle forces and the uplift of the Colorado Plateau, *Geophys. Res. Lett.*, *36*, L19310, doi:10.1029/2009GL039778.

Orth, C. P., and V. S. Solomatov (2012), Constraints on the Venusian crustal thickness variations in the isostatic stagnant lid approximation, *Geochem. Geophys. Geosyst.*, *13*, Q11012, doi:10.1029/2012GC004377.

Pérez-Campos, X., Y. Kim, A. Husker, P. M. Davis, R. W. Clayton, A. Iglesias, J. F. Pacheco, S. K. Singh, V. C. Manea, and M. Gurnis (2008), Horizontal subduction and truncation of the Cocos Plate beneath central Mexico, *Geophys. Res. Lett.*, *35*, L18303, doi:10.1029/2008GL035127.

Petersen, R. I., D. R. Stegman, and P. J. Tackley (2016), The subduction dichotomy of strong plates and weak slabs, *Solid Earth Discuss.*, *2016*, 1–23.

Pusok, A. E., and B. J. P. Kaus (2015), Development of topography in 3-D continental-collision models, *Geochem. Geophys. Geosyst.*, *16*, 1378–1400, doi:10.1002/2015GC005732.

Ribe, N. M., and U. Christensen (1999), The dynamical origin of Hawaiian volcanism, *Earth Planet. Sci. Lett.*, *171*(4), 517–531.

Ribe, N. M., and U. R. Christensen (1994), Three-dimensional modeling of plume-lithosphere interaction, *J. Geophys. Res.*, *99*(B1), 669–682.

Rodríguez-González, J., A. M. Negredo, and M. I. Billen (2012), The role of the overriding plate thermal state on slab dip variability and on the occurrence of flat subduction, *Geochem. Geophys. Geosyst.*, *13*, Q01002, doi:10.1029/2011GC003859.

Russell, M., and M. Gurnis (1994), The planform of epeirogeny: Vertical motions of Australia during the Cretaceous, *Basin Res.*, *6*(2–3), 63–76.

Ryan, W. B. F., et al. (2009), Global multi-resolution topography synthesis, *Geochem. Geophys. Geosyst.*, *10*, Q03014, doi:10.1029/2008GC002332.

Schmeling, H., et al. (2008), A benchmark comparison of spontaneous subduction models: Towards a free surface, *Phys. Earth Planet. Int.*, *171*(1–4), 198–223, doi:10.1016/j.pepi.2008.06.028.

Stauder, W. (1973), Mechanism and spatial distribution of Chilean earthquakes with relation to subduction of the oceanic plate, *J. Geophys. Res.*, *78*(23), 5033–5061.

Suarez, G., T. Monfret, G. Wittlinger, and C. David (1990), Geometry of subduction and depth of the seismogenic zone in the Guerrero gap, Mexico, *Nature*, *345*(6273), 336–338.

Tackley, P. J. (2008), Modelling compressible mantle convection with large viscosity contrasts in a three-dimensional spherical shell using the yin-yang grid, *Phys. Earth Planet. Int.*, *171*(1–4), 7–18, doi:10.1016/j.pepi.2008.08.005.

Taramón, J. M., J. Rodríguez-González, A. M. Negredo, and M. I. Billen (2015), Influence of cratonic lithosphere on the formation and evolution of flat slabs: Insights from 3-D time-dependent modeling, *Geochem. Geophys. Geosyst.*, *16*, 2933–2948, doi:10.1002/2015GC005940.

Thielmann, M., B. Kaus, and A. Popov (2015), Lithospheric stresses in Rayleigh–Bénard convection: Effects of a free surface and a viscoelastic Maxwell rheology, *Geophys. J. Int.*, *203*(3), 2200–2219.

van Hunen, J., A. P. van den Berg, and N. J. Vlaar (2004), Various mechanisms to induce present-day shallow flat subduction and implications for the younger Earth: A numerical parameter study, *Phys. Earth Planet. Int.*, *146*(1–2), 179–194.

Vlaar, N., and M. Wortel (1976), Lithospheric aging, instability and subduction, *Tectonophysics*, *32*(3–4), 331–351.

Watanabe, T., M. G. Langseth, and R. N. Anderson (1977), Heat flow in back-arc basins of the Western Pacific, in *Island Arcs, Deep Sea Trenches and Back-Arc Basins*, pp. 137–161, AGU, Washington, D. C.

Wheeler, P., and N. White (2002), Measuring dynamic topography: An analysis of Southeast Asia, *Tectonics*, *21*(5), 1040, doi:10.1029/2001TC900023.

Zhong, S., and M. Gurnis (1992), Viscous flow model of a subduction zone with a faulted lithosphere: Long and short wavelength topography, gravity and geoid, *Geophys. Res. Lett.*, *19*(18), 1891–1894.

Zhong, S., and M. Gurnis (1994), Controls on trench topography from dynamic models of subducted slabs, *J. Geophys. Res.*, *99*(B8), 15,683–15,695.